JGR Solid Earth

RESEARCH ARTICLE
10.1029/2024JB029649

Evidence for Lithospheric Mantle Uniformity Beneath Cratons

Federico D. Munch[1], **Paolo A. Sossi**[2], **and Amir Khan**[1,2]

[1]Institute of Geophysics, ETH Zurich, Switzerland, [2]Institute of Geochemistry and Petrology, ETH Zurich, Switzerland

Key Points:

- We propose a new model chemical system that captures the compositional variability recorded in mantle xenoliths
- The lithospheric composition of cratonic roots is independent of cratonic age
- The asthenospheric mantle beneath cratons is ~50°C cooler than ambient mantle

Supporting Information:

Supporting Information may be found in the online version of this article.

Correspondence to:

F. D. Munch,
federico.munch@eaps.ethz.ch

Citation:

Munch, F. D., Sossi, P. A., & Khan, A. (2025). Evidence for lithospheric mantle uniformity beneath cratons. *Journal of Geophysical Research: Solid Earth*, *130*, e2024JB029649. https://doi.org/10.1029/2024JB029649

Received 19 JUN 2024
Accepted 31 MAR 2025

Author Contributions:

Conceptualization: Federico D. Munch, Paolo A. Sossi, Amir Khan
Formal analysis: Federico D. Munch, Paolo A. Sossi
Funding acquisition: Amir Khan
Methodology: Federico D. Munch, Amir Khan
Writing – original draft: Federico D. Munch, Paolo A. Sossi, Amir Khan

Abstract Cratons are characterized by thick mantle roots that have experienced high degrees of partial melting, resulting in a cold, strong, and buoyant mantle compared to its oceanic counterpart. The extent of chemical variability within cratonic roots, the role of cratons in insulating the mantle over time and subsequent triggering of continental break-up, however, remains debated. To better understand the lithospheric and asthenospheric compositional variability of cratons, we combine phase equilibrium computations with the inversion of P-to-s and S-to-p receiver function waveforms and fundamental-mode Rayleigh wave dispersion data recorded at 53 globally distributed seismic stations in different tectonic settings with a focus on cratonic regions. Because existing binary basalt-harzburgite models are unable to account for the variability in Mg# (MgO/[MgO + FeO]) and Mg/Si ratios recorded in xenoliths from cratonic regions, we propose an extension of the binary model that is based on nominally pyroxenite, lherzolite and dunite. The retrieved mantle lithospheric compositions have elevated Mg# (~90–93) compared to asthenospheric mantle (Mg# ~89), consistent with their having undergone differing degrees of melt extraction at mean pressures of 3–4 GPa. There are no indications for systematic differences in mantle composition or thermal structure with craton age or location. Instead, we find that the potential temperature of the asthenosphere beneath cratons is roughly 50°C cooler than the surrounding ambient mantle. This suggests that the insulating (i.e., heating) effect of continents may not be as prominent as implied by dynamical studies simulating the exchange of heat and material across the mantle.

Plain Language Summary Cratons are the oldest building blocks of the Earth's crust and are thought to be supported by cold, strong, and buoyant mantle (i.e., roots). However, the degree of chemical variability within cratons remains unclear. By combining different types of seismic data and a new methodology to translate these data into estimates of temperature and composition of the cratonic roots, we find that the roots are (a) chemically buoyant because of melt extraction, (b) their composition does not vary with age, and (c) the mantle below cratonic roots is relatively cold.

1. Introduction

The lithospheric and sub-lithospheric mantle are complex physicochemical systems that interact via mass and energy transfer processes over various length and time scales. Such interactions largely control the evolution of tectonic and geological processes (e.g., Braun, 2010; Coltice et al., 2017; Korenaga, 2018). In particular, cratons are characterized by roots that have experienced very high degrees of partial melting and melt removal (Boyd & McCallister, 1976), which results in a cold, strong, and buoyant mantle compared to its oceanic counterpart (Jordan, 1978). However, the degree of chemical variability of such cratonic roots as well as the extent to which the thermal characteristics of the lithosphere are intrinsically linked to its composition remains poorly understood.

The study of xenoliths (i.e., mantle fragments carried to the surface by volcanic rocks) provides insights into the physical, thermal, compositional, and chronological history of the continental mantle (e.g., Carlson et al., 2005; Griffin et al., 2009; Nixon et al., 1981; Pearson et al., 2021). During partial melting, CaO and Al_2O_3 are preferentially removed from the solid aggregate, whereas MgO increases through the production of olivine below ~2 GPa and orthopyroxene up to ~7 GPa via peritectic melting reactions (Herzberg, 2004b; Kinzler & Grove, 1992). The behavior of FeO is intermediate between these two cases and remains roughly constant in mantle residues. Among these oxides, the Mg# (MgO/[MgO + FeO]), in addition to SiO_2, is particularly indicative because (a) FeO, MgO, and SiO_2 account for ~95% by weight of peridotites; (b) as FeO and MgO are extracted to different degrees during melting episodes, their relative abundances reflect the extent of partial melting; (c) The SiO_2/[MgO + FeO] of a given bulk rock is a first-order control on the relative abundances of the major minerals (i.e., olivine and pyroxene).

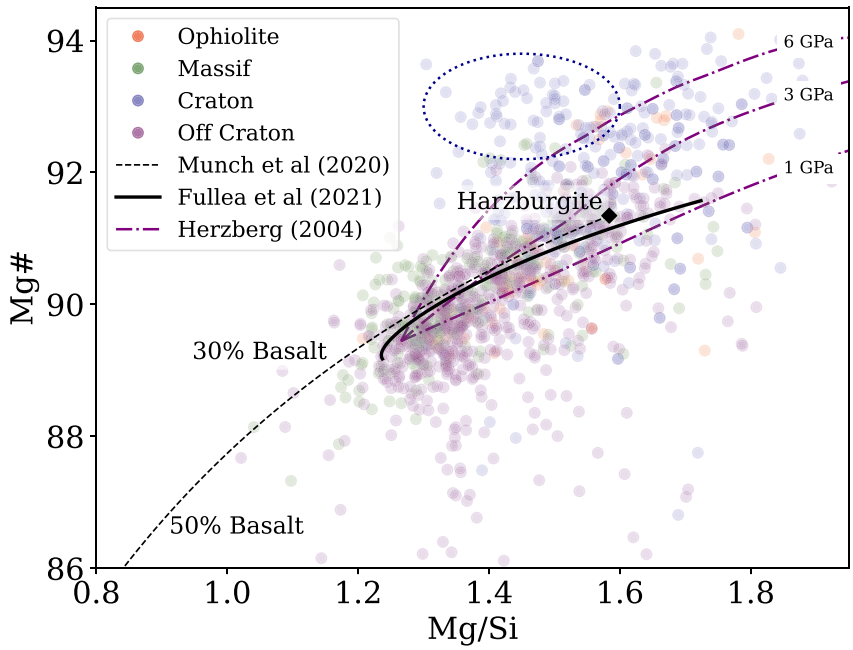

Figure 1. Variability in Mg# (Mg/(Mg + Fe)) and Mg/Si derived from the analysis of mantle peridotites in outcrop and xenoliths (circles) colored-coded by tectonic settings (Canil, 2004). Samples from the Siberian and Kaapval cratons (encompassed by the blue-dotted ellipse) are characterized by an excess in SiO_2 (Boyd et al., 1997) in contrast to samples from other cratonic regions (blue circles). Dash-dotted purple lines illustrate experimentally determined melting curves of peridotite (i.e., residue) at 1, 3, and 6 GPa from Herzberg (2004a). Black lines correspond to chemical models typically used in geophysical studies. Black dashed line illustrates the range of Mg# and Mg/Si for a mantle described as a mixture of basalt and harzburgite (Munch et al., 2020). Black solid line depicts the range covered by a mantle described using Al_2O_3 as the main unknown and scaling relationships based on geochemical abundances to estimate the remaining oxides (Fullea et al., 2021). The chemical model systems by Munch et al. (2020) and Fullea et al. (2021) mimic the trend in off-cratons (magenta), massif (green), and ophiolite (red) samples but cannot predict the high Mg# (≥90) and low Mg/Si ratios at a given Mg # observed in cratonic regions.

During melt extraction, the Mg# of the residue increases almost linearly with the degree of melting, regardless of whether melting is a batch or a fractional process and/or whether it occurs under wet or dry conditions (Hirose & Kawamoto, 1995; Herzberg & O'hara, 2002; Herzberg, 2004b). Moreover, higher pressures have little effect on the relative efficiency of MgO versus FeO extraction, as both are hosted predominantly in olivine and the exchange coefficient is nearly independent of pressure (Toplis, 2005), such that the Mg# is a reliable indicator of the extent of melt extraction undergone by peridotite residues.

Figure 1 summarizes the variability in: (a) Mg# and Mg/Si ratio derived from the analysis of mantle peridotites in outcrop and xenoliths color-coded by tectonic setting (Canil, 2004); and (b) melting curves (purple lines) for peridotite at 1, 3, and 6 GPa (Boyd et al., 1997; Herzberg, 2004a). Mantle xenoliths from cratonic regions (blue circles) show chemical compositions that diverge from those plausibly produced as residues of melt extraction (i.e., magenta lines). In particular, samples from the Siberian and Kaapval cratons (blue-dotted ellipse) are characterized by an excess in SiO_2 (Boyd et al., 1997). Although this Si-enrichment was first believed to be a primary characteristic of Archean subcontinental mantle, lower SiO_2 concentrations were measured in xenoliths from the Slave (Kopylova & Russell, 2000) and North Atlantic (Bernstein et al., 1998) cratons suggesting that Si-enrichment is a secondary (metasomatic) feature imposed upon the subcontinental mantle after its formation as a residue of melting (Carlson et al., 2005). Furthermore, recent analyses of major element data for a suite of peridotite xenoliths in the Udachnaya kimberlite (e.g., Ionov et al., 2010) hint toward the Siberian craton being more similar to the Slave with lower Mg/Si ratios than previously reported. The extent to which these peridotitic xenoliths are representative of the entire mantle lithosphere that underly cratons, and the role of this metasomatism in determining the thermomechanical structure of the lithospheric mantle, however, is at present unclear (e.g., Doucet et al., 2020).

Seismic data can be used to better characterize the composition and thermal structure of the mantle, because melt depletion and metasomatism result in mineralogical changes that manifest as seismic velocity variations. Such changes in material properties can be imaged seismologically and further translated into variations in mantle temperature and major element composition by means of inverse methods and mineral phase equilibria calculations (Afonso et al., 2016; Eeken et al., 2018, 2020; Fullea et al., 2021; Khan et al., 2009; Munch et al., 2018) or by combining laboratory measurements of shear modulus and attenuation (e.g., Priestley & McKenzie, 2013; Priestley et al., 2024). In particular, the analyses of receiver functions provided an excellent tool to study lateral variations in mantle thermochemical structure (Bissig et al., 2021; Calò et al., 2016; Glasgow et al., 2024; Lawrence & Shearer, 2006a, 2006b; Munch et al., 2020; Schmandt, 2012; Tauzin et al., 2008, 2017) as depth and amplitude of seismic discontinuities in the mantle are a function of local temperature, pressure, and composition (Bina & Helffrich, 1994; Helffrich, 2000; Xu et al., 2008).

However, these geophysical models have relied on simplified parameterizations of mantle composition through the assumption of: (a) a uniform pyrolite composition; (b) a basalt–harzburgite mixture based on a chemically equilibrated mantle (Munch et al., 2018; Ritsema et al., 2009) or a mechanical mixture (Xu et al., 2008); (c) the amount of Al_2O_3 as the main unknown supplied with scaling relationships based on geochemical abundances to estimate the amounts of CaO, MgO, and SiO_2 while fixing the amount of FeO (to 8.1 wt % in the lithosphere and 8.05 wt% sub-lithospheric mantle; Afonso et al., 2013; Fullea et al., 2021). As illustrated in Figure 1, these parameterizations (black lines) cannot predict the entire range of Mg# and Mg/Si ratios observed in mantle xenoliths.

In this study, we develop a new, three-component chemical model to account for compositional changes that are otherwise not captured in geophysically derived models of the composition and thermal state of the upper mantle. To test the extended framework, we build and invert receiver function waveforms in combination with existing fundamental-mode dispersion data recorded at 53 stations located in different cratonic regions and non-cratonic settings. We also explore the correspondence between the seismically derived thermo-chemical structure with inferences from the analysis of mantle xenoliths. The new chemical model better captures the compositional diversity observed in cratonic mantle peridotites, in addition to providing a better fit to the seismic data than was possible with the basalt-harzburgite model. Briefly, we find that: (a) the lithospheric mantle beneath modified cratons typically has higher Mg# values (~90–93) compared to Phanerozoic regions, which are characterized by values closer to that of the convecting mantle (~89); (b) there is no systematic correlation between cratonic lithospheric mantle composition and age; and (c) mantle potential temperatures range from 1290 to 1340°C in the oldest Archean regions and up to ~1375°C in younger areas.

2. Mantle Chemical Model

In our previous work (e.g., Bissig et al., 2021; Munch et al., 2018, 2020), mantle composition ($\mathbf{X}$) was described in terms of a single-parameter (f) representing the amount of basalt in a basalt–harzburgite mixture

$$\mathbf{X} = f\,\mathbf{X}_b + (1 - f)\,\mathbf{X}_h, \tag{1}$$

where the compositions of harzburgite ($\mathbf{X}_h$) and basalt ($\mathbf{X}_b$) are described in the CFMASNa model chemical system, comprising the oxides CaO-FeO-MgO-Al_2O_3–SiO_2-Na_2O (see Table 1), and which accounts for ~99% of the mass of Earth's mantle. The rationale for this parameterization is based on the observed chemical trends generated by partial melting of mantle material along mid-ocean ridges, which produces a basaltic crust and its depleted residue (harzburgite) (Xu et al., 2008).

In spite of its simplicity, this two-component model provides a good first-order description of mantle chemistry from a geophysical standpoint (e.g., Bissig et al., 2021; Khan et al., 2009; Khan et al., 2013; Munch et al., 2020; Ritsema et al., 2009; Xu et al., 2008). However, as illustrated in Figure 1, this parameterization is unable to predict the entire range of Mg# and Mg/Si ratios observed in mantle xenoliths. The black lines in Figure 1 delineate Mg# and Mg/Si ratios for harzburgite and basalt end-member compositions used in previous studies (e.g., Munch et al., 2020), illustrating that such a model neither accounts for the high Mg# (≥90) nor the low Mg/Si ratios for a given Mg# observed in cratonic regions (blue circles).

Table 1
Model End-Member Bulk Compositions in wt%

Component	Basalt ($\mathbf{X}_B$)	Harzburgite ($\mathbf{X}_H$)	Dunite* ($\mathbf{X}_{dun^*}$)	Pyroxenite* ($\mathbf{X}_{pyx^*}$)	Lherzolite* ($\mathbf{X}_{lhz^*}$)
CaO	13.05	0.5	0.00	11.50	0.00
FeO	7.68	7.83	6.00	6.00	10.00
MgO	10.49	46.36	53.00	23.00	42.50
Al_2O_3	16.08	0.65	0.00	12.00	0.00
SiO_2	50.39	43.64	41.00	47.50	47.50
Na_2O	1.87	0.01	0.00	0.00	0.00

Note. Basalt and Harzburgite compositions taken from Khan et al. (2009). Dunite-like ($\mathbf{X}_{dun^*}$), Pyroxenite-like ($\mathbf{X}_{pyx^*}$) and Lherzolite-like ($\mathbf{X}_{lhz^*}$) compositions correspond to the end-member system proposed in this study.

To extend the model so that it encompasses the uncovered compositional regions in Figure 1, we propose a new three-component system to describe the composition of the lithospheric mantle ($\mathbf{X}$) as

$$\mathbf{X} = f_{dun^*}\,\mathbf{X}_{dun^*} + f_{pyx^*}\,\mathbf{X}_{pyx^*} + f_{lhz^*}\,\mathbf{X}_{lhz^*}, \tag{2}$$

where f_{dun^*}, f_{lhz^*}, and f_{pyx^*} represent the fractional amounts of dunite-, lherzolite-, and pyroxenite-like end-members, respectively. The composition of the dunite- ($\mathbf{X}_{dun^*}$), pyroxenite- ($\mathbf{X}_{pyx^*}$), and lherzolite-like ($\mathbf{X}_{lhz^*}$) end-members in the CFMASNa model chemical system are summarized in Table 1 and illustrated in Figure 2. The end-member compositions were found by maximizing the number of samples that fall within the

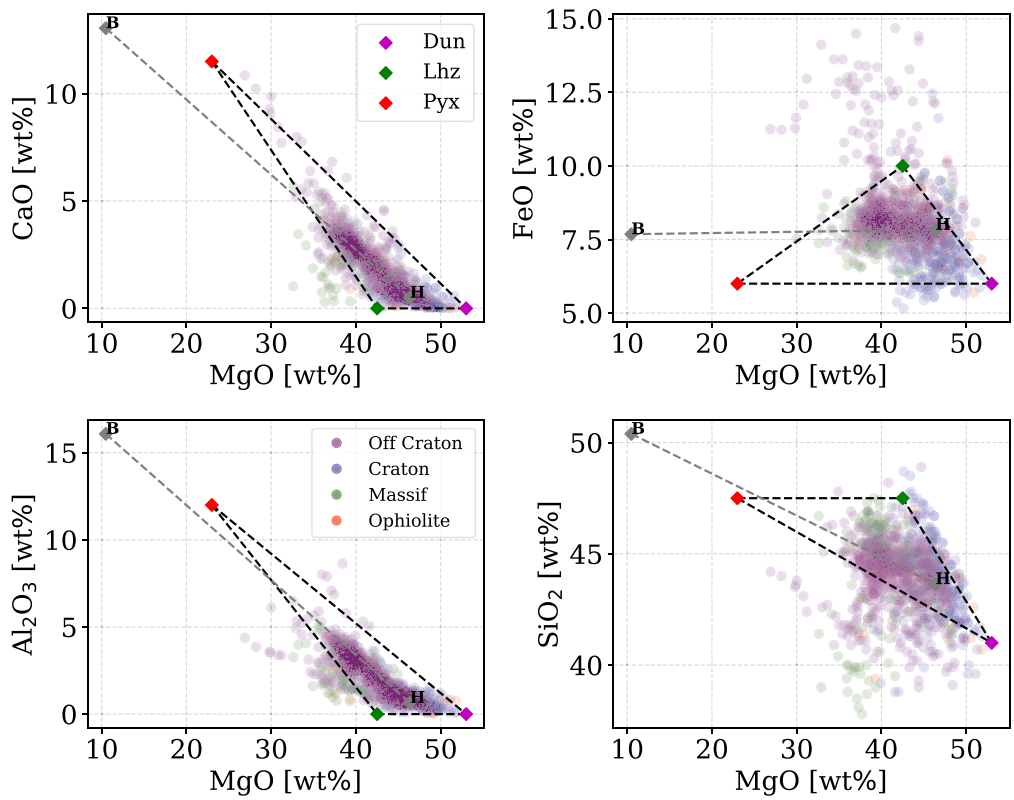

Figure 2. Variability of the main oxides (i.e., MgO, FeO, Al_2O_3, CaO, and SiO_2) observed in mantle xenoliths (circles) color-coded by tectonic settings (Canil, 2004). Gray dashed lines indicate the portion of the compositional space covered by a mantle described as a mixture of basalt (B) and harzburgite (H) as used by Munch et al. (2020). Colored diamonds depict the composition of the three end-members (Dun, Pyx, Lhz) proposed in this study (see Section 2). The best-fitting multi-dimensional triangles (dashed black lines) encompass: (1) 72% of the ophiolite samples; (2) 81% of the massif samples; (3) 65% of the cratonic samples; and (4) 73% of the off-cratonic samples present in the database of Canil (2004).

multi-dimensional triangles shown in Figure 2, so as to encompass as much of the diversity present in natural peridotitic samples (Canil, 2004). To this end, we performed a gridsearch over the compositional space (with grid-spacing equal to 0.5 wt%) with the constraint that each proposed end-member composition should sum to 100 wt% (i.e., $f_{dun^*} + f_{pyx^*} + f_{lhz^*} = 1$). The amount of Na_2O oxide in the proposed composition was set to zero as the amounts of this oxide in natural samples are not available in the database.

Figure 2 illustrates the portion of the compositional space covered by the proposed three-component system (black dashed triangles) and the variability recorded in natural samples (circles). The best-fitting multi-dimensional triangles (dashed black lines in Figure 2) enclose: (a) 72% of the ophiolite samples; (b) 81% of the massif samples; (c) 65% of the cratonic samples; and (d) 73% of the off-cratonic samples present in the database of Canil (2004). In comparison to a basalt-harzburgite chemical model (gray dashed lines), the three-component system not only captures the main (linear) trends, but also 73% of the diversity present in natural samples. This is reflected in the range of Mg# numbers and Mg/Si ratios modeled by the new three-component system (see Figure S1 in Supporting Information S1).

3. Inversion of Seismic Data for Mantle Thermo-Chemical Structure

As a means of testing the three-component chemical model proposed here, we jointly invert P-to-s and S-to-p receiver function (RF) waveforms and Rayleigh wave fundamental-mode dispersion data recorded at stations located in different tectonic settings for the thermo-chemical properties of the lithospheric mantle. The different data sets are complementary in that they are sensitive to different parts of the model: P-to-s and S-to-p RFs are sensitive to crust and lithospheric structure, respectively, whereas the Rayleigh wave dispersion data provide information on the absolute wave speeds of crust and upper mantle, particularly vertically polarized S-wave velocities. In what follows, we briefly describe the seismic data, the model parameterization, seismic forward modeling, that is, prediction of RF waveforms and phase velocity dispersion data, and finally how we solve the inverse problem.

3.1. Seismic Data

P-to-s and S-to-p RFs are the records of compressional and shear waves that convert into shear and compressional waves, respectively, when encountering a sharp discontinuity in seismic properties underneath a seismic station (e.g., Rondenay, 2009). The fundamental concept behind the construction of receiver functions is to separate signals generated by the direct and converted phases on three-component ground-motion measurements based on their distinct particle motion (Kind et al., 2012; Rondenay, 2009). For a P-to-s conversion, the direct P-wave motion is recorded on the vertical component, while the converted S-wave is observed on the radial component. The order is reversed for S-to-p conversions. The converted signal can be understood as the convolution of the direct wavefield with the local structural response. Hence, deconvolving the direct phase from the converted phase results in a time series that represents the structure below the receiver (Langston, 1979; Vinnik, 1977). This deconvolution operation is considered to remove the source and path effects between event and conversion points (Kind et al., 2012).

We construct a high-quality data set of P-to-s and S-to-p receiver function waveforms recorded at 53 broad-band seismic stations that are globally distributed across different cratonic and non-cratonic settings (see Figure 3). To this end, we acquire seismic data between 2002 and 2022 from the NSF SAGE datacenter (ds.iris.edu/ds/nodes/dmc/) via ObspyDMT (Hosseini & Sigloch, 2017) and event information from the global centroid moment tensor catalog (www.globalcmt.org; Dziewonski et al., 1981; Ekström et al., 2012). Only events with a magnitudes large than 5.5 and a focal depth shallower than 150 km are considered. The later is necessary to reduce the interference of S-to-p conversions with surface-reflected multiples (Wilson et al., 2006). Following our previous work (e.g., Bissig et al., 2021), we select epicentral distances between 40°–95° and 55°–90° for the P-to-s and S-to-p RFs, respectively.

Seismic waveforms are then filtered between 0.02 and 1 Hz using a Butterworth bandpass filter of second order and rotated to the vertical-radial-transverse system. In the case of the S-to-p RFs, we perform a second rotation to the LQT system, where the orthogonal L and Q components are roughly aligned with the S and S-to-p converted phases, respectively (Kind et al., 2012; Rondenay, 2009). The orientation of the L and Q axes is determined by means of principal component analysis to maximize the energy in the window from −30 to +50 s on the Z/L component around the theoretical S-wave arrival (Bissig et al., 2021). To ensure high-quality data, we only

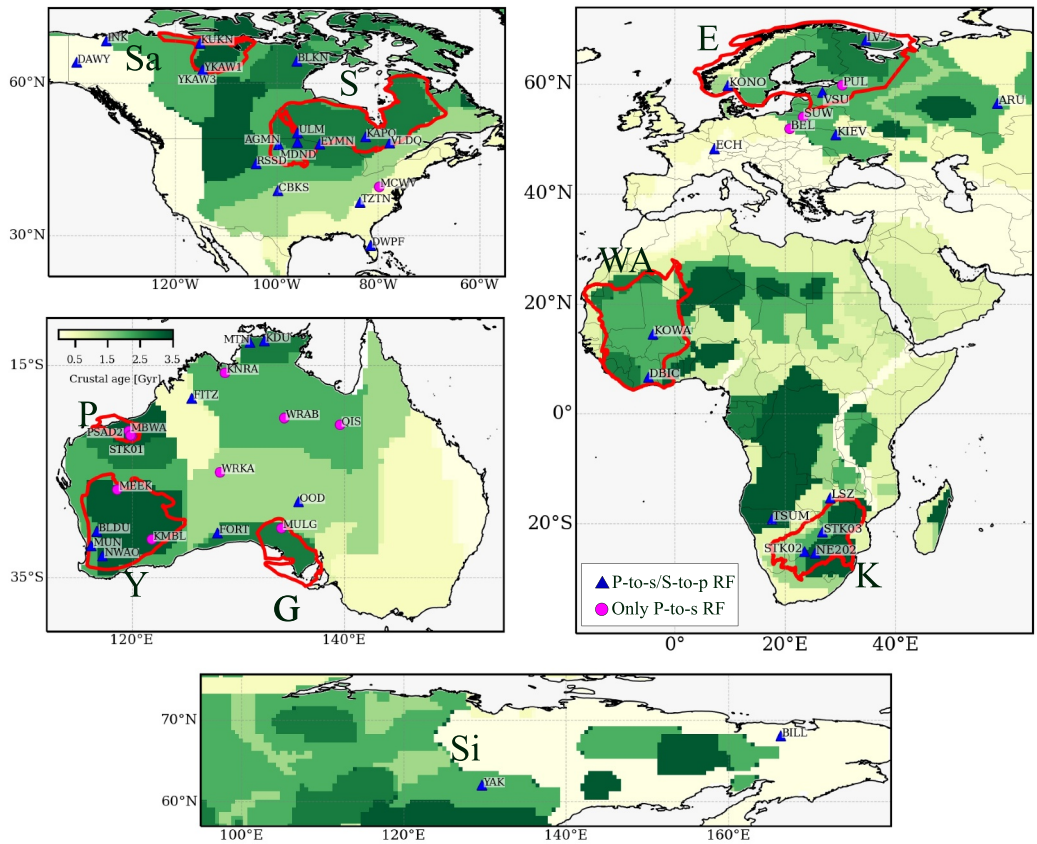

Figure 3. Geographic location of broad-band seismic stations considered in this study, blue triangles denote stations for which both P-to-s and S-to-p receiver function (RF) data are available, while magenta circles indicate locations with only P-to-s RF waveforms. Background color depicts tectono-thermal ages from Artemieva (2006) excluding oceans. Red solid contours indicate major cratonic units: Superior (S), Slave (Sa), European (E), Kalahari (K), West African (WA), Pilbara (P), Gawler (G), and Yilgarn (Y). Station Yakutia (YAK) is located within the Siberian (Si) craton (contour not shown in the map).

consider waveforms with a signal-to-noise ratio (SNR) larger than 5. RFs are then obtained by applying an iterative time-domain deconvolution (Ligorria & Ammon, 1999) on the direct phase (i.e., window between −50 and +150 s for the P-to-s RFs; and between −100 and +30 s the S-to-p RFs) and the converted signals (i.e., window from −50 to +150 s and from −150 to +50 s for P-to-s and S-to-p RFs, respectively). Finally, we apply a move-out correction to a reference slowness (i.e., 6.5 s/° for P-to-s and 9.9 s/° for S-to-p RFs) and filter the stacked RFs in the period range 5–100 s (P-to-s) and 10–100 s (S-to-p). Errors on stacked amplitudes are estimated using a bootstrap resampling approach (Efron & Tibshirani, 1991). The time axis and polarity of S-to-p RFs are flipped to facilitate the comparison with the P-to-s RFs.

In order to increase the SNR ratio in areas where only few (≤20) events were recorded (e.g., South Africa and North West Australia), we stacked the receiver function waveforms from stations located within a ∼100 km radius (labeled STK01, STK02, STK03). The SNR of S-waves is typically lower than for P-waves because of interfering phases, which generally complicates the observation of S-to-p conversions. As a result, the amplitudes of P-wave multiples between the surface and the mantle transition zone can become significant to the extent that these can be mistaken for conversions (Bock, 1994; Wilson et al., 2006). This requires careful inspection of the S-to-p RF waveforms. After removal of low SNR stacks by visual inspection of the waveforms, our final data set consists of 53 P-to-s and 39 S-to-p stacked receiver functions for stations located in the Superior, Slave, European, Kalahari, West African, Pilbara, Gawler, Yilgarn and Siberian cratons as well as off-cratonic regions. Figure 3 summarizes locations where both P-to-s and S-to-p (triangles) and only P-to-s (circles) RF waveforms are available.

Table 2
Overview of Model Parameters and Prior Model Parameter Ranges

Description	Parameter	Number of unknowns	Range
Crustal structure			
Thickness (km)	d^i	3	1–20
S-wave velocity of first layer (km/s)	V_s^i	1	2.0–4.1
S-wave velocity change (km/s)	δV_s^i	2	0–0.75
Density-to-S wave velocity ratio	ρ/V_s	1	0.7–0.9
P-to-S wave velocity ratio	V_p/V_s	1	1.7–1.9
Lithospheric thermal structure			
Base temperature (°C)	T_{lit}	1	1350–1450[a]
Thickness (km)	z_{lit}	1	80–275
Curvature of geotherm	α	1	$0–T_{lit}/z_{lit}^2$
Composition			
Lithospheric mantle			
Lherzolite-like end-member fraction	f_{lhz^*}	1	0–1.00
Pyroxenite-like end-member fraction	f_{pyx^*}	1	0–0.40
Dunite-like end-member fraction	f_{dun^*}	Fixed	$1-(f_{lhz^*}+f_{pyx^*})$
Asthenospheric mantle			
Basalt fraction	f	1	0–0.40

[a]The temperature range encompasses temperature estimates derived from models of primary magmas from non-arc basalts (Herzberg & Gazel, 2009).

Finally, we complemented our receiver function data set with surface-wave data to better constrain upper mantle velocity structure (e.g., Bissig et al., 2021; Munch et al., 2020; Priestley et al., 2024). For this purpose, we extracted fundamental-mode Rayleigh wave phase-velocity dispersion curves for each station from the phase-velocity maps of Durand et al. (2015) using a nearest-neighbor interpolation scheme. This data set provides fundamental-mode phase-velocity data, including uncertainties, for 13 periods between 40 and 200 s.

3.2. Model Parameterization

Based on previous experience (e.g., Bissig et al., 2021; Munch et al., 2018, 2020), we model the subsurface beneath each station as consisting of a crust and mantle that are further parameterized in terms seismic wave velocities and thermo-chemical parameters, respectively. Table 2 summarizes model parameters and prior ranges considered in the inversion (see Section 3.5). Owing to the low temperatures that inhibit equilibration by solid-state diffusion, vast portions of the continental crust are likely to be out of thermodynamic equilibrium. As a result, the mineralogical assemblage of crustal rocks are likely decoupled from the in-situ pressure and temperature conditions. Consequently, the velocity structure of the crust is modeled as a stack of three layers with variable S-wave velocity $\left(V_s^i\right)$, thickness $\left(d^i\right)$, and constant density- and P-to-S wave velocity ratios (ρ/V_s and V_p/V_s). Velocity jumps in the crust $\left(\delta V_s^i\right)$ are assumed to be positive.

The mantle parameterization is illustrated in Figure 4 and consists of lithospheric and asthenospheric temperature T and composition. Temperature is described by a conductive geotherm in the lithosphere that connects to a mantle adiabat beneath (Shapiro & Ritzwoller, 2004). Assuming steady-state conditions and a constant volumetric heat production with depth, the temperature in the lithosphere (see Appendix A) can be expressed as

$$T(z) = \left(\frac{T_{lit}-T_{surf}}{z_{lit}}+\alpha z_{lit}\right)z-\alpha z^2 \quad \text{for } z<z_{lit}, \tag{3}$$

where z_{lit} denotes lithospheric thickness, and T_{surf} and T_{lit} are temperature at the surface (0°C) and the base of the lithosphere, respectively. The dimensionless parameter α—defined as the volumetric heat production to thermal

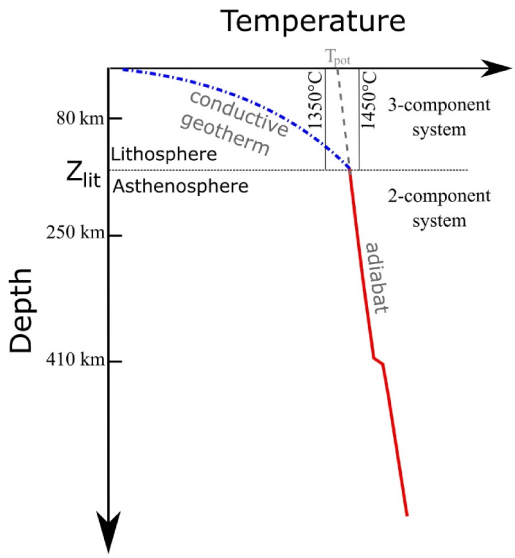

Figure 4. Sketch of thermal and compositional parameterization used in this study. Mantle temperature is described by a conductive geotherm (blue) on top of an adiabat (red). Mantle adiabats (i.e., isentropes) are self-consistently calculated from the entropy of the lithology at depth z_{lit} (i.e., bottom of conductive lithosphere) and a temperature of 1400°C ± 50°C (Section 3.2). Mantle potential temperature T_{pot}—equivalent to the temperature that a parcel of mantle would have at the surface, if it ascended along an adiabat without undergoing melting (McKenzie & Bickle, 1988)—is computed by extrapolating the adiabat to the surface (gray dashed line). Lithospheric mantle composition (i.e., depth < z_{lit}) is described using the three-component model proposed in this study (see Section 2), while asthenospheric mantle composition is described in terms of the 2-component (i.e., harzburgite-basalt) model.

conductivity—controls the concavity of the conductive profile and is allowed to range from 0 (linear geotherm) to a maximum value (see Appendix A). Mantle adiabats are self-consistently computed from the entropy of the lithology at the temperature T_{lit} and pressure P_{lit} at the bottom of the conductive lithosphere. Pressure is computed by integrating the load from the surface. Model parameters and prior model parameter ranges are discussed further in Section 3.5 and listed in Table 2.

This particular thermal parameterization allows us to represent continents as conductive lids floating on top of the convective mantle and to easily compute the mantle potential temperature T_{pot}—which is equivalent to the temperature that a parcel of mantle would have at the surface, if it ascended along an adiabat without undergoing melting (McKenzie & Bickle, 1988)—by extrapolating the adiabatic part of the thermal profile to the surface (see dashed gray line in Figure 4). However, it should be mentioned that the resulting geotherms could potentially have more curvature than expected for a scenario where heat production in the crust is much (e.g., an order of magnitude) higher than in the lithospheric mantle (e.g., Priestley & McKenzie, 2006). However, since our framework relies on a seismic parameterization in the crust, its thermal structure is unresolved. Within the sublithospheric mantle, self-consistent isentropes are computed from the entropy of the lithology at the base of the lithosphere.

For composition, the mantle beneath each station is parameterized in terms of a lithospheric and an asthenospheric composition (Figure 4). Lithospheric mantle composition is defined by means of the three-component model proposed in this study (Section 2), whereas asthenospheric mantle is described in terms of the amount of basalt f in a basalt-harzburgite mix because—as discussed in Section 2—it provides a good first-order description of asthenospheric mantle chemistry from a geophysical point of view (e.g., Bissig et al., 2021; Khan et al., 2013; Munch et al., 2020; Ritsema et al., 2009; Xu et al., 2008).

3.3. Determining Anelastic Seismic Wave Velocities

Equilibrium modal mineralogy, isotropic (infinite-frequency) seismic wave velocities and density as a function of composition, pressure, and temperature are computed using `Perple_X` (Connolly, 2009) for which the thermodynamic formulation and data of Stixrude and Lithgow-Bertelloni (2011) is employed. The predicted mineralogy depends on the degree of equilibration between the end-members, with two mixing models proposed (Xu et al., 2008): equilibrium assemblage (EA) and mechanical mixture (MM). The former implies full equilibration, while the MM model considers the mantle to be a mixture of the end-members. Here, we focus on the EA model as synthetic modeling (see Figures S2 and S3 in Supporting Information S1) indicates that the seismic data here considered have low sensitivity to differences between the MM and EA models. Uncertainties in elastic moduli and density estimated using Gibbs energy minimization are ~2%–3% and ~0.5%–1%, respectively (Connolly & Khan, 2016). Effects related to redox conditions and the presence of water and melt are neglected here because of lack of thermodynamic data.

To consider anelastic effects on seismic amplitudes and surface wave dispersion data, we rely, as in our previous work (e.g., Bissig et al., 2021; Munch et al., 2018, 2020), on the extended Burgers model, which is a laboratory-based dissipation model derived from grain-size-, temperature-, and pressure-sensitive viscoelastic relaxation measurements of anhydrous melt-free polycrystalline olivine (Jackson & Faul, 2010; Lau & Faul, 2019). Radial profiles of shear attenuation and relaxed shear moduli are determined using the implementation of Bagheri et al. (2019) with the rheological parameters listed in Table S1 of Supporting Information S1. Shear attenuation is truncated at an upper limit of 300, whereas bulk attenuation is fixed at 57,823 after PREM (Dziewonski & Anderson, 1981). The advantage of this setup is that it allows for a direct link of the petrologically predicted (i.e.,

unrelaxed) shear moduli with the appropriate creep function (see Appendix B), wherefrom relaxed shear moduli at the periods required for modeling RF waveforms (1 s) and surface wave dispersion data (100 s) can be obtained.

Alternative laboratory-based viscoelastic models, including Maxwell, Andrade, Sundberg-Cooper, and a power law scheme, have been proposed (e.g., Jackson & Faul, 2010; McCarthy et al., 2011; Sundberg & Cooper, 2010; Takei et al., 2014). Bissig et al. (2021) considered the influence of variations in viscoelastic model by comparing the seismic (P-to-s and S-to-p) RF response of the extended Burgers and the Sundberg-Cooper models but found little difference under the assumption that the viscoelastic parameters (Table S1 in Supporting Information S1) were kept constant. Figure S4 in Supporting Information S1 illustrates shear-wave attenuation profiles for the extended Burgers model for grain sizes varying between 0.1 and 50 mm. While the attenuation profiles show small differences in uppermost mantle structure, the fundamental-mode Rayleigh wave phase velocities and P-to-s and S-to-p RFs lack sensitivity to discriminate grain-size. Based on these results, we fix grain-size to 1 mm and keep the remaining viscoelastic parameters as in Table S1 of Supporting Information S1. We leave it to a future study to consider the influence of the various parameters (Table S1 in Supporting Information S1) on seismic velocities and, in turn, seismic response in a more systematic way.

3.4. Computing the Seismic Response

The resulting velocity and attenuation profiles are subsequently used to compute synthetic receiver function waveforms and fundamental-mode Rayleigh wave phase velocities. As detailed in Munch et al. (2018), RF waveform inversion requires that (a) the processing scheme applied to the observed waveforms is duplicated in detail for the modeled waveforms and (b) the observed and modeled slowness distributions at each station are similar. To ensure this, we computed RF waveforms with the reflectivity method (Fuchs & Müller, 1971; Muller, 1985). Surface wave dispersion data are calculated using the spectral element-based python toolbox `specnm` of Kemper et al. (2022).

To study the sensitivity of different thermo-chemical parameters on modeled S-wave velocity profiles and associated seismic response functions (RF waveforms and surface wave dispersion), we computed seismic properties for a range of compositions and geotherms. The results are shown in Figures S5–S8 of Supporting Information S1. The parameters that most significantly influence S-wave velocity and, consequently, seismic response functions are lithospheric temperature, thickness, and composition, whereas asthenospheric composition appears least significant. While crustal properties are also important in this regard, a detailed overview of their effect on P-to-s and S-to-p RF waveforms is given in Bissig et al. (2021).

We may note that the waveform modeling performed here is based on an isotropically layered model and, as a result, is unable to account for material anisotropy and diffraction effects related to three-dimensional mantle structure. In spite of these apparent limitations, we should note that the present 1-D waveform RF synthetics have been verified against 3-D full waveform RF synthetics and showed good agreement (Bissig et al., 2021). Consequently, the 1-D approach results in reliable P-to-s and S-to-p RFs. Finally, we ignore radial anisotropy and assume that vertically polarized S-wave speeds (V_{SV}) are equivalent to the isotropic S-wave speeds (V_S) computed here (Section 3.3). Presently, this is an acceptable approximation as indicated in Figure S9 of Supporting Information S1, which shows vertically polarized S-wave speeds for different degrees of radial anisotropy (1%–10%) and corresponding seismic response functions (RFs and surface-wave dispersion curves) for the case where $V_S = V_{SV}$, inasmuch as for the anisotropy range considered, the variability in the seismic response is seen to lie within the uncertainties of the data.

3.5. Solving the Inverse Problem

To infer variations in mantle temperature and composition beneath each station, we invert the RF waveforms and Rayleigh wave phase-velocity data using the model parameterization and forward operators described in the previous sections. Deterministic derivative-based methods (e.g., Gauss-Newton) could be applied, however, these techniques typically depend on the choice of initial model and are prone to converge to a local minimum. Following our previous work (e.g., Munch et al., 2018), we solve the inverse problem within a Bayesian framework using the probabilistic approach of Tarantola and Valette (1982) to overcome the limitations of deterministic methods.

In the Bayesian formulation, the solution to the general inverse problem $\mathbf{d} = g(\mathbf{m})$, where $\mathbf{d}$, $\mathbf{m}$ and g denote data, model and forward operator, respectively, is given in terms of the posterior probability distribution $\sigma(\mathbf{m}) \propto \rho(\mathbf{m})\mathcal{L}(\mathbf{m})$. Here, $\rho(\mathbf{m})$ represents the a priori probability distribution on model parameters (described in Section 3.2 and summarized in Table 2) and $\mathcal{L}(\mathbf{m})$ is the likelihood function, which represents a measure of the similarity between observed data $\mathbf{d}$ and the predictions from model $\mathbf{m}$.

Modeled and observed RF waveforms are compared in specific time windows, which are defined by visual inspection of the observed waveforms. For the P-to-s RFs, the time windows encompass: (a) crustal signal ($-5\text{ s} < t < 30\text{ s}$) and (b) the P410s, that is, the P-wave converted to an S-wave at the 410-km seismic discontinuity, which is typically recorded in the time window 40 s–50 s. For the S-to-p RFs, the time window encompasses conversions from the Moho and the lithosphere-asthenosphere boundary ($-5\text{ s} < t < 30\text{ s}$). Under the assumption that data noise can be modeled using a L_2-norm, the likelihood function $\mathcal{L}(\mathbf{m})$ can be written as

$$\mathcal{L}(\mathbf{m}) \propto \exp\left\{-\frac{1}{2}\left[\phi^{\mathrm{Ps}}(\mathbf{m}) + \phi^{\mathrm{Sp}}(\mathbf{m}) + \phi^{\mathrm{SW}}(\mathbf{m})\right]\right\}, \tag{4}$$

where $\phi^{\mathrm{Ps}}(\mathbf{m})$, $\phi^{\mathrm{Sp}}(\mathbf{m})$ and $\phi^{\mathrm{SW}}(\mathbf{m})$ are the misfit functions associated with P-to-s RFs, S-to-p RFs and surface wave phase velocities, respectively, which are given by

$$\phi^{\mathrm{Ps}}(\mathbf{m}) = \frac{1}{2}\sum_{i=1}^{2}\frac{1}{\mathrm{N}_{\mathrm{Ps}}^{\mathrm{i}}}\sum_{j=1}^{\mathrm{N}_{\mathrm{Ps}}^{\mathrm{i}}}\left[\frac{\mathbf{d}_{\mathrm{Ps}}^{\mathrm{obs}}(t_j) - \mathbf{d}_{\mathrm{Ps}}^{\mathrm{syn}}(t_j)}{\sigma_{\mathrm{Ps}}(t_j)}\right]^2, \tag{5}$$

$$\phi^{\mathrm{Sp}}(\mathbf{m}) = \frac{1}{\mathrm{N}_{\mathrm{Sp}}}\sum_{j=1}^{\mathrm{N}_{\mathrm{Sp}}}\left[\frac{\mathbf{d}_{\mathrm{Sp}}^{\mathrm{obs}}(t_j) - \mathbf{d}_{\mathrm{Sp}}^{\mathrm{syn}}(t_j)}{\sigma_{\mathrm{Sp}}(t_j)}\right]^2, \tag{6}$$

and

$$\phi^{\mathrm{SW}}(\mathbf{m}) = \frac{1}{\mathrm{N}_{\mathrm{SW}}}\sum_{k=1}^{\mathrm{N}_{\mathrm{SW}}}\left[\frac{\mathbf{d}_{\mathrm{SW}}^{\mathrm{obs}}(T_k) - \mathbf{d}_{\mathrm{SW}}^{\mathrm{syn}}(T_k)}{\sigma_{\mathrm{SW}}(T_k)}\right]^2, \tag{7}$$

where $\mathbf{d}^{\mathrm{obs}}$ and $\mathbf{d}^{\mathrm{syn}}$ represent observed and modeled P-to-s and S-to-p RF waveforms and surface wave phase velocities, respectively, σ denotes observational uncertainties for each data type (estimated as described in Section 3.1) and N_{Ps} and N_{Sp} are the number of samples in the P-to-s and S-to-p time windows (t_j), respectively, and N_{SW} the number of periods (T_k).

The posterior distribution in the model space, $\sigma(\mathbf{m})$, is obtained through a two-step procedure: we first apply a stochastic optimization technique (CMAES; Hansen et al., 2011) to explore the model space globally and find a model that explains the observations within uncertainties. Following this, we apply a Metropolis-Hastings Markov chain Monte Carlo (McMC) method as a means of sampling the model space for better uncertainty quantification (e.g., Mosegaard & Tarantola, 1995) using the solution retrieved from the CMAES algorithm as starting model. This significantly reduces the burn-in time of the McMC algorithm, whereby its efficiency is considerably improved. The McMC sampling stage is performed using 5 independent chains (20,000 iterations per chain) with the same CMAES starting model but different randomly chosen initial perturbations with an overall acceptance rate in the range 14%–34%. Finally, the 10,000 best-fitting candidates are used to build histograms of the marginal probability distribution of each model parameter.

4. Results

4.1. Fit to the Data

Figure 5 illustrates the fit between the observed (black) and inverted (red) receiver function waveforms and surface wave dispersion data for five stations located in the Superior craton. Individual figures showing the data fit for each station can be found in Figures S10–S62 of Supporting Information S1. The inverted models successfully mimic the observed P-to-s conversions for 39 seismic stations (blue diamonds in Figure S63 in

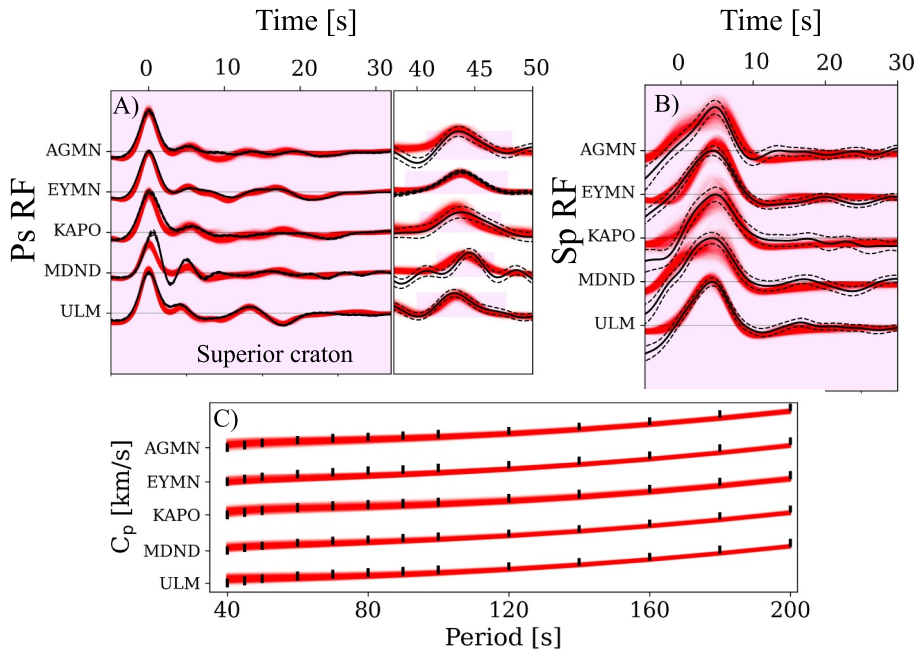

Figure 5. Example of fit between observed (black) and inverted (red): (a) P-to-s receiver functions (RFs), (b) S-to-p RFs, and (c) fundamental-mode Rayleigh wave phase velocities C_p for five stations in the Superior craton. Observations and uncertainties are shown as black solid and dashed lines, respectively. Pink rectangles indicate the part of the RF waveforms that is fitted in the inversion. For improved visibility, amplitudes of P-to-s conversions at the 410-km discontinuity (i.e., time window 35–50s) are scaled up. Individual data fits for all stations are shown in Figures S10–S62 of Supporting Information S1.

Supporting Information S1), of which 27 also show good agreements between observations and predictions for the S-to-p conversions. Similarly, the retrieved models successfully reproduce the variability present in the surface wave dispersion data set. As generally observed in the case of S-to-p RFs (e.g., Bissig et al., 2021; Yuan et al., 2006), the SNR is lower than P-to-s RFs, as a result of which S-to-p RFs are not as well-matched as P-to-s RFs. In particular, we find a subset of 14 stations with poor fit to the S-to-p RF waveforms (e.g., ARU and FITZ; Figures S10 and S21 in Supporting Information S1) that are located both in cratonic and off-cratonic regions (red triangles in Figure S63 of Supporting Information S1). These stations were excluded from further analysis.

4.2. Influence of Chemical Model on the Retrieved Thermo-Chemical Structure

In order to assess the influence of the proposed model chemical system on the retrieved mantle thermo-chemical structure, we inverted the geophysical data using the basalt-harzburgite mixture model considered in our previous work (Munch et al., 2020). As summarized in Figure S64 of Supporting Information S1, the use of the three-component chemical model leads to an overall reduction (of up to 15%) in misfit relative to the solutions obtained with a pure two-component (basalt-harzburgite) model. Figure 6 summarizes the main differences in the retrieved compositional (panels A–C) and thermal (panels D–F) parameters obtained using the two- and three-component models. To quantify the degree of similarity between the two- and three-component solutions, we computed the Pearson correlation coefficient (PCC). We find that the use of the two-component model restricts the inferred ranges of lithospheric Mg# (~89–91) and Mg/Si (~1.15–1.45), while the three-component system allows for significantly more variability with Mg# numbers ranging between 88 and 93 and Mg/Si ratios between 1.15 and 1.70, respectively. This leads to very low PPC values (0.11 and 0.04) for these two parameters. Although there is a slight correlation between lithospheric composition and thickness (see Figure S65 in Supporting Information S1), the inverted thermal structure does not appear to be significantly influenced by the choice of mantle compositional model (see Figures 6d–6f).

The formation and preservation of compositional heterogeneity in the Earth's mantle has a strong effect on global mantle convection patterns and controls the long-term evolution of geochemical reservoirs (e.g., Yan et al., 2020). In our previous work (e.g., Munch et al., 2020), we suggested the presence of significant variability in

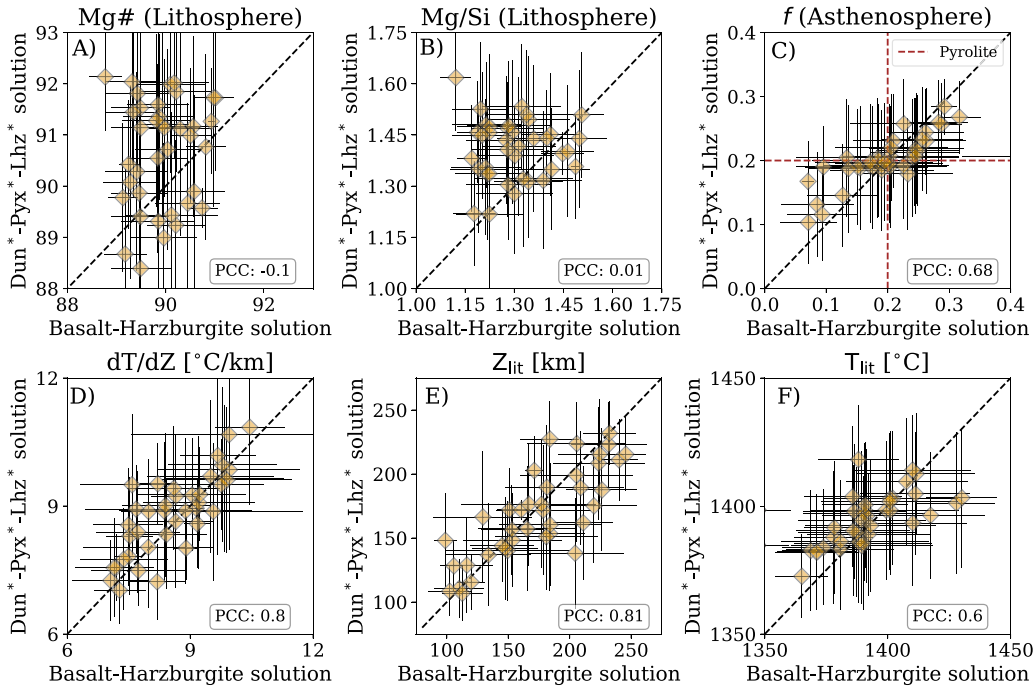

Figure 6. Best-fitting values and Pearson correlation coefficient (PCC) of lithospheric (a) Mg# and (b) Mg/Si ratios, (c) asthenospheric basalt fraction f, (d) lithospheric thermal gradient dT/dz at 75 km depth, (e) lithospheric thickness z_{lit}, and (f) temperature at the base of the lithosphere T_{lit} inferred from the seismic data by using the three-component system with Dun*, Pyx*, and Lhz* being the dunite-, pyroxenite-, and lherzolite-like compositions proposed in this study, and the basalt-harbuzgite model to describe the composition of the lithospheric mantle. Diamonds indicate medians of each model parameter and black lines depict the associated standard deviations. Red dashed line in Panel C ($f = 0.20$) illustrates pyrolitic mantle composition.

asthenospheric mantle composition between cratonic and Phanerozoic regions based on the analysis of P-to-s RFs and surface wave dispersion data. That analysis relied on the two-component model and the assumption of a compositionally homogeneous mantle beneath each station, raising the question as to whether the retrieved variations are truly representative of the asthenospheric mantle or merely result from the use of a single layer to describe mantle composition.

Figure 6c shows a comparison between best-fitting asthenospheric mantle compositions obtained using the two- and three-component systems, respectively. The large PCC (0.68) suggests that the variability reported by Munch et al. (2020), where basalt fraction ranges from 0.05 to 0.35, is a robust feature of the asthenospheric mantle and is unlikely to reflect changes in lithospheric composition. This strengthens the growing evidence for large lateral variations in upper mantle composition from the analysis of surface wave dispersion data (e.g., Fullea et al., 2021; Khan et al., 2009; Meier et al., 2009), receiver functions (e.g., Bissig et al., 2021; Glasgow et al., 2024; Schmandt, 2012; Tauzin et al., 2008; Zhang et al., 2022), PP/SS precursors (e.g., Bissig et al., 2023; Chambers et al., 2005; Tauzin et al., 2022; Tian et al., 2020; Waszek et al., 2021) and triplicated P- and S-waveforms (e.g., Bissig et al., 2022; Borgeaud et al., 2019; Grand, 2002). Overall, these results emphasize the importance of accounting for mantle compositional variations in the inversion of seismic data, as opposed to what has been recently advocated by Lebedev et al. (2024) on the basis of seismic velocities being primarily controlled by thermal variations. To show that this is unlikely to provide a satisfactory match to data, we performed a set of inversions, where we fixed mantle composition to pyrolite and inverted for temperature. Not surprisingly, this resulted in an overall (5%–40%) increase in misfit (see Figure S66 in Supporting Information S1).

4.3. Comparison With Global Models

Figure 7 compares the best-fitting Moho depths, mantle temperatures at 100 and 250 km depths, respectively, and lithospheric thicknesses beneath each station against predictions from the global models CAM2022 (Priestley et al., 2024), WINTERC-G (Fullea et al., 2021), and LITHOREF18 (Afonso et al., 2019). CAM2022

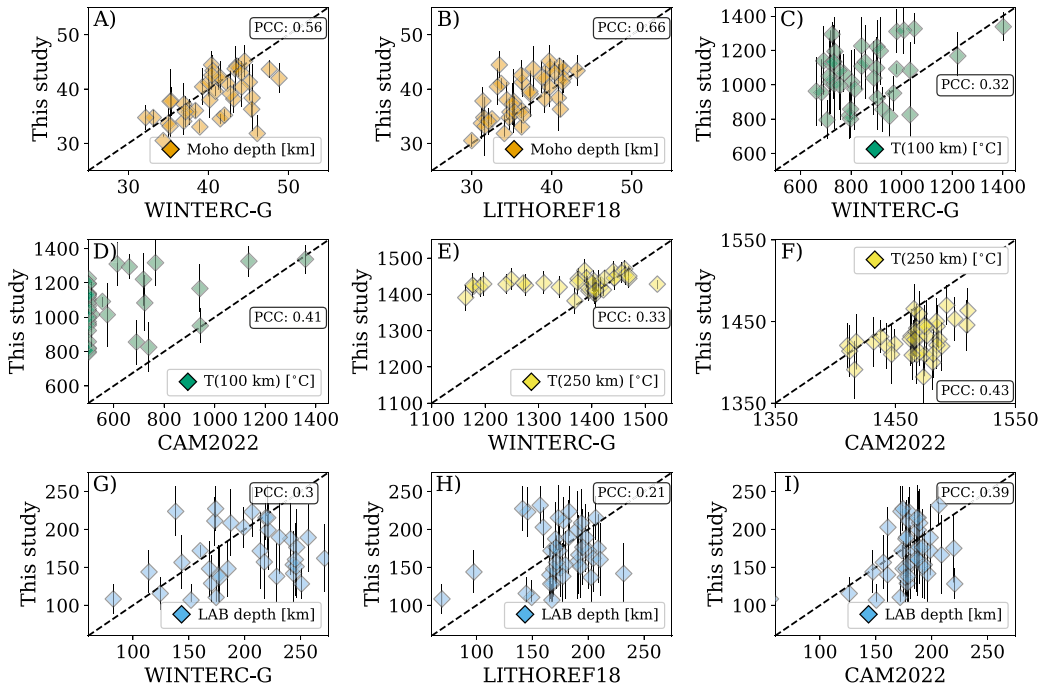

Figure 7. Best-fitting crustal thickness and thermal structure estimates from this study and predictions from global models CAM2022 (Priestley et al., 2024), WINTERC-G (Fullea et al., 2021), and LITHOREF18 (Afonso et al., 2019). Panels show variations in (a–b) Moho depth, (c–d) temperature (T) at 100 km depth, (e–f) T at 250 km depth, and (g–i) depth of the lithosphere-asthenosphere boundary (LAB). To facilitate the comparison, we computed the Pearson correlation coefficient (PCC). To simplify visualization, low temperatures in panel D are saturated to 500°C. Diamonds correspond to the mean of the best-fitting solutions derived in this study and solid lines denote standard deviations.

is a global tomographic and thermal model derived from the inversion of fundamental- and higher-mode surface waveforms (Priestley & McKenzie, 2013; Priestly et al., 2024). WINTERC-G is a global thermo-chemical model of the upper mantle derived from the inversion of fundamental-mode Love and Rayleigh waves phase velocities, gravity anomalies, geoid heights, satellite-derived gravity gradients, and surface heat flow and elevation. LITHOREF18 is a global model of crustal and upper mantle density structure obtained from the inversion of gravity anomalies, geoid height, satellite-derived gravity gradients, and elevation with constraints on crustal thickness based on the global crustal model CRUST1.0 (Laske et al., 2013) and on lithospheric thickness based on six tomographic models.

To first order, the recovered Moho depths (Figures 7a and 7b) are in overall agreement with estimates from WINTERC-G and LITHOREF18, as reflected in the large PCC values. Significant differences, however, exist in mantle temperatures, where model WINTERC-G predicts ∼100°C cooler temperatures at 100 km, while cratonic regions are characterized by anomalously cold mantle temperatures (i.e., ≤500°C) in model CAM2022 (Figures 7c and 7d). As discussed by Priestley et al. (2024, see Section 2), the latter results from the use of a velocity-to-temperature conversion (Priestley & McKenzie, 2006) based on V_{sv} rather than on V_s. These modeling-related artifacts diminish with depth such that our estimates are in overall agreement with temperatures in CAM2022 at 250 km depth, although slightly warmer (∼50°C) mantle temperatures are suggested CAM2022 (Figures 7e and 7f). In comparison, temperature variations at 250 km depth underneath cratons are anomalously large (∼350°C) in model WINTERC-G relative to temperature estimates derived from the analyses of mantle xenoliths (see Section 5.1). This could be partially attributed to the inability of their compositional model (solid line in Figure 1) to account for the chemical variability recorded by mantle xenoliths from cratonic regions.

The differences in inferred thermal structure discussed above also affect the thermal lithosphere-asthenosphere boundary (LAB). As illustrated in Figures 7g–7i, lithospheric thicknesses in model LITHOREF18 typically do not exceed 210 km in cratonic regions, while the RF data considered here suggests the presence of up to 250 km thick cratonic roots in localized areas. The low correlation with model LITHOREF18 (PCC ∼ 0.2) could be related to lithospheric thicknesses in LITHOREF18 being derived from potential field data, which are insensitive

to discontinuities. Our lithospheric thickness estimates correlate slightly better with those of model CAM2022 (PCC ∼ 0.39) and WINTERC-G (PCC ∼ 0.3). However, model CAM2022 suggests a smaller variation in LAB thickness (180–220 km) beneath cratons relative to our estimates and model WINTERC-G (∼120–250 km). Discrepancies in upper bounds between our estimates and model CAM2022 may be related to the latter defining the LAB based on a mantle potential temperature of 1,315°C instead of 1,350°C. Differences in the minimum LAB thickness could be attributed to modeling-related artifacts in CAM2022 that, as shown above, affect the lithospheric thermal structure beneath cratons.

5. Discussion

5.1. Comparison With Pressure-Temperature Estimates From Xenoliths

Mineral thermobarometry enables the reconstruction of the temperature profile for the whole depth column from which the xenoliths are derived by linking rock composition to pressure and temperature with a mineral thermobarometer (e.g., Boyd, 1973; Pearson et al., 2003). In general, stable cratons are characterized by cold geotherms (with temperatures ranging between 750°C and 900°C at 100 km depth or roughly 3 GPa, following a 35–38 mWm^{-2} conductive geotherm; Finnerty & Boyd, 1987), with the coldest temperatures found in Archean cratons (Boyd et al., 1997; Kopylova et al., 1999) and only slightly warmer geotherms beneath long, stable sections of Proterozoic crust (e.g., Boyd et al., 2004; Eggler et al., 1987; Finnerty & Boyd, 1987; Jaques et al., 1990). Particularly hot, sheared garnet peridotite xenoliths from the Kaapvaal record temperatures between 1,050°C to 1,250°C between 4.4 and 6.5 GPa (Lazarov et al., 2009), respectively, and, together, define a conductive geotherm of 40–41 mWm^{-2}, only marginally lower than the 42 mWm^{-2} inferred for younger regions of the Kalahari craton (e.g., Kimberley, Lesotho; Bell et al., 2003; Woodland & Koch, 2003), which are also truncated at shallower depths (∼180 km). Xenoliths from the surrounding Proterozoic mobile belts yield higher temperatures at a given pressure with surface heat flow around 55 ± 17 mWm^{-2} (e.g., Bell et al., 2003; Nyblade & Pollack, 1993). Such a difference is typically attributed to the combination of increased crustal heat production (Morgan, 1984) and a thinner mantle lithosphere (e.g., Ballard & Pollack, 1987).

Together, these petrological observations indicate generally cool, lithospheric mantle underlying Archean cratons, whereas the mantle beneath tectono-magmatically active continental regions (e.g., Shorttle et al., 2014) tends toward much hotter geotherms (i.e., temperatures ≥1,000°C at 100 km depth) even in areas where crustal ages are old such as the Central African Rift in Tanzania (Lee & Rudnick, 1999) and the Baikal Rift in Russia (Ionov, 2002). The range of thermal variations in the shallow continental mantle derived by xenolith thermobarometry seems to be in overall agreement with inferences made from the analysis of seismic velocities in tomographic models (e.g., Ball et al., 2021; Bissig et al., 2021; Cammarano et al., 2009) and electrical conductivity profiles (e.g., Artemieva, 2006). However, the extent to which geotherms recorded by xenoliths are indeed steady-state conductive geotherms or represent transient conditions present at the time the xenoliths were brought to the surface remains debated (Bell et al., 2003; Doucet et al., 2014; Harte & Freer, 1982). Moreover, the degree to which these xenoliths are representative of the thermo-compositional structure of the cratonic mantle is uncertain, making seismological data invaluable in illuminating their regional characteristics.

Figure 8 shows upper and lower bounds of best-fitting temperature profiles to the seismic data for the: (a) Superior; (b) Gawler; and (c) Siberian cratons for stations close to mines/sources of mantle xenoliths. Equivalent panels for the European, Pilbara, Yilgarn, Kalahari, Slave, and West African cratons are shown in Figure S67 of Supporting Information S1. Figure 8 also depicts a compilation of thermobarometer estimates of the $P - T$ conditions recorded by individual xenoliths (circles) for each region (Garber et al., 2018). We find a good overlap between seismically derived and thermobarometry-based geotherms, in particular for the Gawler craton (emplacement ages ∼189 Ma). However, present-day geotherms for the Siberian (emplacement ages ∼160 Ma) and Superior (emplacement ages ∼632 Ma) cratons are sightly warmer by ∼75°C and ∼100°C, respectively, hinting toward potential heating processes associated with lithospheric thinning and asthenospheric upwelling in these cratons (e.g., Qin et al., 2024). The differences reported here are larger than the uncertainties associated with the precision of the typical garnet-orthopyroxene and garnet-clinopyroxene thermobarometers applied to these rocks (±60°C and 0.45 GPa; Nimis & Grütter, 2010; Tappert et al., 2011). Thus, our results support the notion that the geotherms recorded by xenoliths represent transient conditions present at the time the samples were brought to the surface rather than steady-state conductive geotherms, at least for the Superior and Siberian cratons.

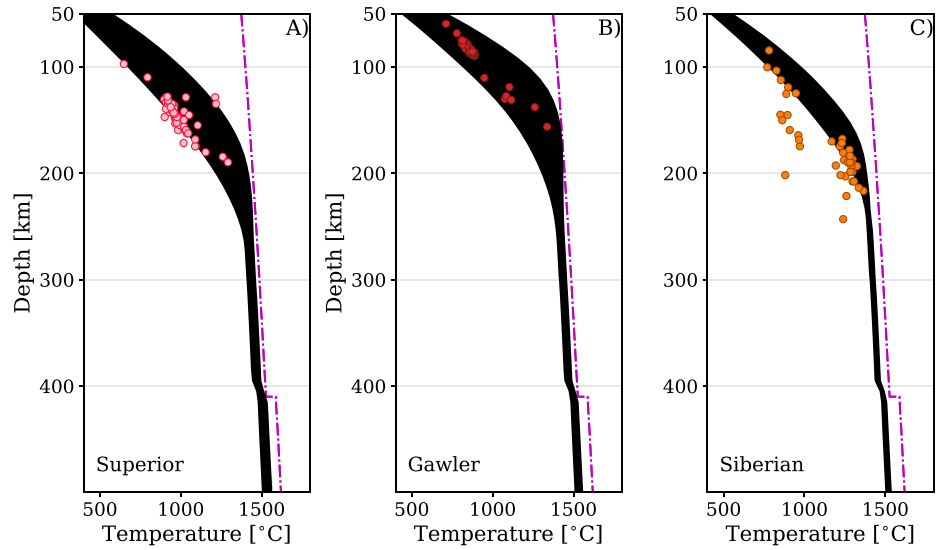

Figure 8. Upper and lower bounds of best-fitting temperature profiles (gray) for the: (a) Superior (USA, emplacement ages ~632 Ma), (b) Gawler (Australia, emplacement ages ~189 Ma), and (c) Siberian (Russia, emplacement ages ~160 Ma) cratons. Colored circles illustrate thermobarometry-based geotherms for each region (Garber et al., 2018). The dashed (magenta) line denotes the experimentally determined average mantle (adiabatic) thermal profile of Katsura (2022).

5.2. Thermal Evolution of the Subcratonic Mantle

Continents influence mantle dynamics by modulating the heat flow at the Earth's surface (e.g., Jain et al., 2019; Lenardic et al., 2011). On the one hand, craton formation, through melt extraction, leads to removal of heat-producing elements (U, Th, K) by virtue of their incompatibility during mantle melting (e.g., Sun & McDonough, 1989). In a closed system, this would result in older cratons having cooler geotherms owing to (a) the decrease in internal heat production and (b) loss of heat advectively upon melt segregation. On the other hand, the stability of cratons is undermined by continual metasomatism via traversing melts over time (Menzies & Hawkesworth, 1986), leading to the deposition of advective heat, but also radiogenic heat from incompatible elements. Furthermore, it has been proposed that continents can act as thermal insulators by inhibiting heat loss and shielding the subcontinental mantle from cold, down-going slabs, thus increasing mantle temperatures regionally over time (Anderson, 1982; Ballard & Pollack, 1987; Cooper et al., 2006; Gurnis & Hager, 1988; Lenardic et al., 2005, 2011; Lenardic & Moresi, 2001). For instance, 3-D mantle convection simulations with various continental configurations predict an increase of ~140°C in mantle potential (i.e., asthenospheric) temperature underneath continents relative to the sub-oceanic mantle in ~200 Myr (Jain et al., 2019; Rolf et al., 2012). On the other hand, Heron and Lowman (2011) investigated the effect of continental insulation in 3-D mantle convection models featuring mechanically and thermally distinct continental and oceanic plates and concluded that averaged subcontinental mantle temperatures do not significantly exceed sub-oceanic temperatures on timescales relevant to super-continent assembly.

In order to test the relative importance of these processes, we examine whether there are spatio-temporal differences in asthenospheric mantle temperature. Figure 9 summarizes best-fitting mantle potential temperature T_{pot} and lithospheric thickness z_{lit} as a function of crustal age, with diamonds indicating mean values of model parameters. Crustal ages were extracted from the $1° \times 1°$ grid of Artemieva (2006) and represent the ages of the last major tectonic event (tectono-thermal ages). Thus, the crust and lithospheric mantle are assumed to share the same age, as supported by Re–Os dating of mantle-derived cratonic xenoliths (Pearson, 1999).

We find mantle potential temperatures ranging from 1,290 to 1,340°C in the oldest Archean regions (see Figure 9a) up to around 1,375°C in younger areas (≤1 Gyr). However, there are no indications for systematic differences with craton age nor between cratons (see Figure S68 in Supporting Information S1). Furthermore, Figure 9c highlights a broad, negative correlation between z_{lit} and T_{pot}, in which young (<1 Gyr), off-cratonic regions define high T_{pot} at low z_{lit}. Because the temperature of the lithosphere-asthenosphere boundary (T_{lit}) is, by construction, restricted to a narrow range (~100°C) in the model and the asthenosphere is approximated to follow

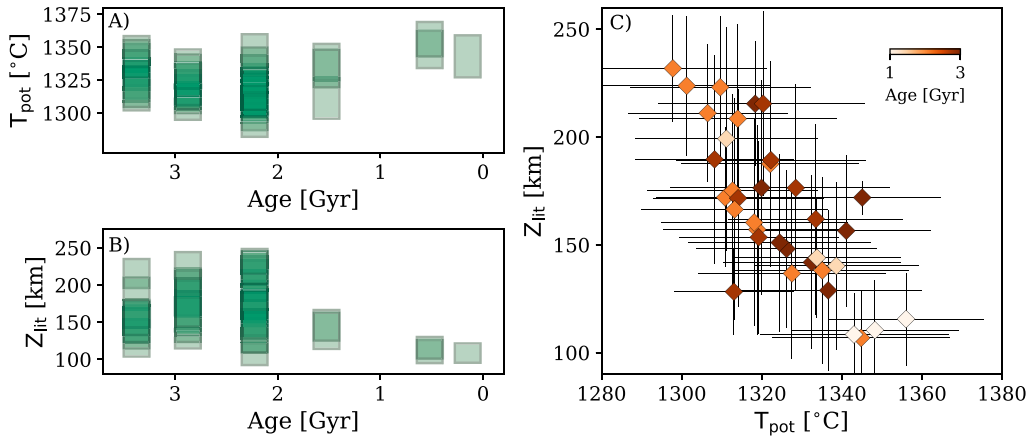

Figure 9. Best-fitting (a) mantle potential temperatures (T_{pot}) and (b) lithospheric thickness (z_{lit}) as a function of age (Artemieva, 2006). Rectangles indicate 50% credible intervals (i.e., interval in which each parameter has a given 50% probability) for each station, with darker colors indicating overlapping estimates. (c) T_{pot} and z_{lit} color-coded by age, with diamonds denoting mean values and black lines illustrate one standard deviation.

an adiabat, a negative correlation between T_{pot} and z_{lit} is expected. Nevertheless, the correlation implies that asthenospheric temperatures beneath cratons (red and orange points) are ~50°C *cooler* than those under off-cratonic regions (white points). This may indicate that, dynamically, volumes of warm mantle are preferentially funneled into regions of thin lithosphere and are diverted away from cratonic regions by their thick continental roots (cf. Duvernay et al., 2022). This temperature offset extends down to the transition zone, the region down to which the seismic data are sensitive. Consequently, the role of continents in limiting heat loss and shielding underlying asthenospheric mantle from potential sources of cooling, such as subduction, is likely not efficient at the scale of the present-day configuration of the plates. Indeed, much larger supercontinents may be required to engender a heating effect beneath cratons (e.g., Heron & Lowman, 2011; Phillips & Bunge, 2005).

5.3. Chemical Variability Within Cratons

Figure 10 summarizes 50% credible intervals (CIs) of best-fitting lithospheric Mg# and Mg/Si ratios (a) color-coded by tectono-thermal age and (b) clustered by craton. Diamonds in panel A represent the mid-point of the CIs and black lines indicate its upper and lower bounds. Green circles represent natural samples and red dashed

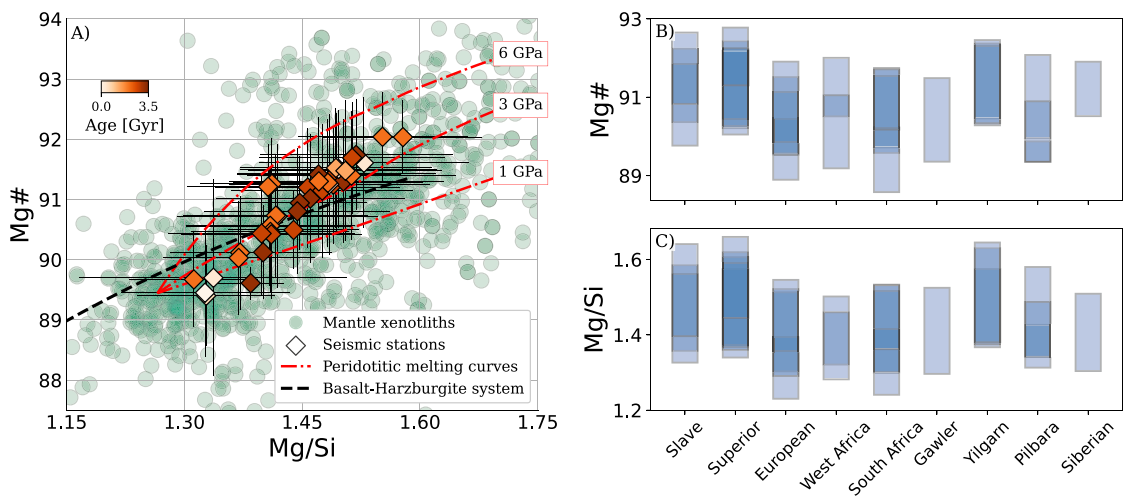

Figure 10. Best-fitting lithospheric Mg# and Mg/Si ratios (a) color-coded by tectono-thermal age (Artemieva, 2006) and (b)–(c) clustered by cratonic region. Black lines and boxes denote 50% credible intervals (CIs) and diamonds in Panel a correspond to the mid-point of each CIs. Similarly to Figure 1, circles depict natural samples (Canil, 2004), red lines indicate melting curves for peridotite at 1, 3, and 6 GPa (Herzberg, 2004a) and dashed black line illustrates the region of the space covered by the basalt-harzburgite chemical model (Munch et al., 2020).

lines indicate peridotitic melting curves at different pressures. The new geophysically derived lithospheric Mg# and Mg/Si ratios (see Figure 10a) show modified cratons typically having higher Mg# values (~90–93) compared to Phanerozoic regions, which are characterized by values closer to the convecting mantle (~89). The notion that cold continental lithosphere is depleted in FeO (i.e., equivalent of a high Mg#) and has higher Mg/Si ratios (~1.2–1.4), relative to the oceanic lithosphere, is commonplace in the petrological literature (e.g., Lee & Rudnick, 1999) and has been further supported by geophysical studies (e.g., Fullea et al., 2021; Khan et al., 2009). Furthermore, the retrieved lithospheric Mg# and Mg/Si ratios are in good agreement with predictions for residues of melt extraction at mean pressures between 3 and 4 GPa (i.e., slightly higher values than expected for the present-day mantle) in agreement with the higher mantle potential temperatures characteristic of the Archean (Arndt et al., 2009; Herzberg, 2004a).

The absence of high Mg# in regions younger than ~500 Ma suggests that the formation of highly melt-depleted peridotites waned after this time (see also Pearson et al., 2021), perhaps owing to mantle cooling. It should be noted that mantle residues produced in some Phanerozoic regions are as depleted as cratonic peridotites, despite being less vertically extensive (~100 km). This may indicate that craton-forming events are not singular, but rather result from the accretion of melt-depleted terranes that thicken to form stable cratons over time.

The lithospheric mantle underneath cratons is mainly described by Mg# ranging between 90 and 93, without systematic differences based on the age of the cratons (see Figure 10a and Figure S69 in Supporting Information S1). We only find subtle differences between cratons with the Slave, Superior, and Yilgarn cratons having slightly higher Mg# (i.e., 90.5–93) compared to other cratonic regions (see Figure 10b). Such differences are narrower than the ones present in mantle xenoliths. For instance, our estimates for the Gawler and Kalahari cratons (89.5–91.5; see Figure 10b) are in agreement with estimates derived from the analysis of surface wave and geodetic data (i.e., $89.2 < \text{Mg\#} < 90.1$; Fullea et al., 2021). However, these values are lower than Mg# recorded in natural samples (i.e., 92–93) for the Kalahari/Kaapvaal. These discrepancies between geophysically derived and xenolith-based atomic ratios are likely attributable to: (a) different depth sensitivities of the seismic and xenolith data sets; (b) the notion that the high Mg# and silicate enrichment captured by natural samples might reflect a localized process rather than a global feature as suggested by recent studies of mantle peridotites (e.g., Doucet et al., 2014, 2020); or (c) presence of compositional stratification in the mantle (e.g., Lee et al., 2011). For instance, the analysis of xenocrystic peridotite minerals disaggregated during magmatic ascent suggests that the Kalahari/Kaapvaal and Slave cratons are dominated by highly melt-depleted peridotites ($\text{Mg\#} \sim 93$) at depths ≤ 150 km, while more fertile lithologies ($\text{Mg\#} \sim 90$) dominate at greater depths (Griffin et al., 2003). Our findings hint toward these features being rather a localized characteristic of cratons, however, future work should focus on: (a) applying the new three-component model to data from dense global arrays (e.g., Glasgow et al., 2024); (b) exploring additional geophysical data sets to further enhance the sensitivity to the lithospheric structure; and (c) extending our framework to self-consistently model crustal thermo-chemical structure and radial variations in lithospheric composition.

6. Conclusions and Outlook

In comparison to the analysis of mantle xenoliths, geophysical techniques provide a more spatially extensive view of the nature of the sub-continental lithospheric mantle. However, current inversions of seismic data for mantle thermo-chemical structure generally rely on a simple binary basalt-harzburgite mixture to describe mantle composition (e.g., Munch et al., 2020) which cannot replicate the compositional variability recorded in xenoliths from cratonic regions. In order to overcome this limitation, we proposed a three-component chemical model that captures the compositional variability in natural samples and applied it to inversion of a newly built data set of P-to-s and S-to-p receiver function waveforms and fundamental-mode Rayleigh wave dispersion data recorded at 53 globally distributed stations covering different tectonic settings.

The new three-component model successfully mimics the compositional diversity observed in cratonic mantle peridotites as it allows for significantly more variability both in Mg# (88–94) and Mg/Si ratios (1.15–1.60). In agreement with the analysis of xenoliths, we find that the lithospheric mantle beneath modified cratons typically has higher Mg# values (~90–93) compared to Phanerozoic regions, which are characterized by values closer to the convecting mantle (~89). Our estimates suggest that the Si-enrichment that was first believed to be a primary characteristic of Archean sub-continental mantle might reflect a localized process rather than a global feature as suggested by recent studies of mantle peridotites (Doucet et al., 2014, 2020). Moreover, we do not find any

systematic correlations between the composition of the lithospheric mantle beneath cratons and its age, suggesting a common process operated throughout the Archean to stabilize such cratons.

In terms of thermal structure, we find mantle potential temperatures ranging from 1,290 to 1,340°C in the oldest Archean regions and up to around 1,375°C in younger areas (≤1 Gyr). This suggest that the asthenosphere beneath cratons remains cold compared to that beneath non-cratonic regions, down to the top of the transition zone, complementing previous work that focussed on non-cratonic regions (Munch et al., 2020). These results possibly indicate that the insulating (i.e., heating) effect of continents may not be as pronounced as predicted by mantle convection simulations.

The extended framework proposed here represents a significant step forward toward the comprehensive analysis of geophysical and petrological observations. For instance, we envision that future work will focus on: (a) the use of compositional variability recorded in local mantle xenolith as prior information in the geophysical inversion; and (b) the inference of radial variations in lithospheric composition as suggested by the analysis of xenocrystic peridotite minerals disaggregated during magmatic ascent. Such analyses suggest the presence of highly melt-depleted peridotites (Mg# ∼ 93) at depths ≤150 km, while more fertile and metasomatized lithologies (Mg# ∼ 90) dominate at greater depths (Griffin et al., 2003). Detailed characterization of such fertile layers (at depths ≥ 150 km) is crucial for better understanding re-fertilization processes (e.g., Lee et al., 2011).

Appendix A: Lithospheric Temperature

If lateral variations are neglected, the temperature (T) within the lithosphere is controlled by the 1-D thermal conductivity equation:

$$\frac{\partial T}{\partial t} = \kappa \frac{\partial^2 T}{\partial z^2} + \frac{\kappa}{k} H, \tag{A1}$$

where κ is the thermal diffusivity, t is time, H is the volumetric heat production, and k is the thermal conductivity. For the steady-state case, the equation reduces to

$$\kappa \frac{\partial^2 T}{\partial z^2} = -\frac{H(z)}{k}, \tag{A2}$$

with boundary conditions

$$T|_{\text{surface}} = 0°\text{C} \qquad \text{and} \qquad T|_{z=z_{\text{lit}}} = \text{T}_{\text{lit}}. \tag{A3}$$

Assuming a constant heat production, the temperature is then given by

$$T(z) = -\alpha z^2 + \left(\frac{\text{T}_{\text{lit}}}{\text{z}_{\text{lit}}} + \alpha \text{z}_{\text{lit}} \right) z, \tag{A4}$$

with $\alpha = H/2k$.

To avoid negative thermal gradients, an upper bound on α can be obtained by imposing that the thermal gradient be zero at the bottom of lithosphere, that is,

$$\left. \frac{dT}{dz} \right|_{z=z_{\text{lit}}} = 0 \tag{A5}$$

which implies

$$-2\alpha \text{z}_{\text{lit}} + \left(\frac{\text{T}_{\text{lit}}}{\text{z}_{\text{lit}}} + \alpha \text{z}_{\text{lit}} \right) = 0 \tag{A6}$$

and therefore that

$$\alpha_{\max} = \frac{T_{lit}}{z_{lit}^2}. \tag{A7}$$

Appendix B: The Extended Burgers Model

The frequency-dependent complex compliance $J(\omega)$ for the Extended Burgers Model (EBM) is defined by

$$J(\omega) = J_1(\omega) + iJ_2(\omega), \tag{B1}$$

where the storage J_1 and loss compliance J_2 for are defined by

$$J_1(\omega) = J_U(r)\left\{1 + \frac{\alpha\Delta_B}{\tau_H^\alpha - \tau_L^\alpha}\int_{\tau_L}^{\tau_H}\frac{\tau^{\alpha-1}}{1+\omega^2\tau^2}\,d\tau + \frac{\Delta_P}{\sigma\sqrt{2\pi}}\int_0^\infty \frac{\exp\left\{-\frac{1}{2}[\ln(\tau/\tau_P)/\sigma]^2\right\}}{\tau(1+\omega^2\tau^2)}\,d\tau\right\}, \tag{B2}$$

$$J_2(\omega) = J_U(r)\left\{\frac{\omega\alpha\Delta_B}{\tau_H^\alpha - \tau_L^\alpha}\int_{\tau_L}^{\tau_H}\frac{\tau^{\alpha}}{1+\omega^2\tau^2}\,d\tau + \frac{\omega\Delta_P}{\sigma\sqrt{2\pi}}\int_0^\infty \frac{\exp\left\{-\frac{1}{2}[\ln(\tau/\tau_P)/\sigma]^2\right\}}{1+\omega^2\tau^2}\,d\tau + \frac{1}{\omega\tau_M}\right\}. \tag{B3}$$

The infinite-frequency unrelaxed compliance J_U defines the elastic behavior, while the anelastic behavior consists of a broad plateau and an absorption band. The former is generally represented by a log-normal distribution with relaxation strength Δ_P centered at τ_P with width σ. The other absorption band, with relaxation strength Δ_B, is delimited by lower and upper cutoff times τ_L and τ_H, whose frequency dependence is determined by the exponent α. In the EBM, the Maxwell relaxation time τ_M dominates the dissipation at long periods. The equations for the relaxation times τ_i for the subscript $i \in \{H, L, P, M\}$ is defined by:

$$\tau_i(d_g, E^*, T, V^*, P) = \tau_{iR}\left(\frac{d_g}{d_{gR}}\right)^{m_i}\exp\left[\left(\frac{E^*}{R}\right)\left(\frac{1}{T} - \frac{1}{T_R}\right) + \left(\frac{V^*}{R}\right)\left(\frac{P}{T} - \frac{P_R}{T_R}\right)\right], \tag{B4}$$

where $R = 8.314\ \mathrm{Jmol^{-1}K^{-1}}$ is the gas constant, T temperature, P pressure, d_g grainsize, E^* activation energy, and V^* activation volume. Subscript R denotes the parameters in the reference, that is, laboratory, state. All necessary parameter values are listed in Table S1 of Supporting Information S1.

Data Availability Statement

[**Data**] All seismic data were downloaded through the EarthScope Consortium Web Services, including the following seismic networks: (1) the II (Scripps Institution of Oceanography, 1986); the IU (Albuquerque Seismological Laboratory/USGS, 2014); the *G* (Institut de physique du globe de Paris (IPGP) & École et Observatoire des Sciences de la Terre de Strasbourg (EOST), 1982); the S1 (Michelle Salmon et al., 2011); the AU (Geoscience Australia, 2021); the US (Albuquerque Seismological Laboratory (ASL)/USGS, 1990); the GE (GEOFON Data Centre, 1993); the CN (Natural Resources Canada, 1975); and the TA (IRIS Transportable Array, 2003). [**Software**] Data processing and receiver function construction was done by means of the python packages `obspy` (Hosseini & Sigloch, 2017) and `rf` (Eulenfeld, 2020). Mineral phase equilibria calculations were

performed with the software PerpleX (Connolly, 2009). Synthetic waveforms were computed using the Reflectivity Method (Fuchs & Müller, 1971). Figures were made with Matplotlib (Hunter & Dale, 2007), Numpy (Harris et al., 2020) and SciPy(Virtanen et al., 2020). [**Results**] The best-fitting models and the receiver function waveforms are available in Munch (2024).

Acknowledgments
We are grateful to Luc Doucet and two anonymous reviewers for comments that led to a much improved manuscript. This study was funded by the Swiss National Science Foundation (project 197369). P.A.S was supported by the Swiss National Science Foundation (SNSF) through an Eccellenza Professorship (#203668). Calculations were performed using the ETH Zurich cluster Euler.

References

Afonso, J. C., Fullea, J., Yang, Y., Connolly, J. A. D., & Jones, A. G. (2013). 3-D multi-observable probabilistic inversion for the compositional and thermal structure of the lithosphere and upper mantle. II: General methodology and resolution analysis. *Journal of Geophysical Research: Solid Earth*, *118*(4), 1650–1676. https://doi.org/10.1002/jgrb.50123

Afonso, J. C., Rawlinson, N., Yang, Y., Schutt, D. L., Jones, A. G., Fullea, J., & Griffin, W. L. (2016). 3-D multiobservable probabilistic inversion for the compositional and thermal structure of the lithosphere and upper mantle: III. Thermochemical tomography in the Western-Central US. *Journal of Geophysical Research: Solid Earth*, *121*(10), 7337–7370. https://doi.org/10.1002/2016jb013049

Afonso, J. C., Salajegheh, F., Szwillus, W., Ebbing, J., & Gaina, C. (2019). A global reference model of the lithosphere and upper mantle from joint inversion and analysis of multiple data sets. *Geophysical Journal International*, *217*(3), 1602–1628. https://doi.org/10.1093/gji/ggz094

Albuquerque Seismological Laboratory (ASL)/USGS. (1990). United States national seismic network [Dataset]. *International Federation of Digital Seismograph Networks*. https://doi.org/10.7914/SN/US

Albuquerque Seismological Laboratory/USGS. (2014). Global seismograph network (GSN—Iris/usgs) [Dataset]. *International Federation of Digital Seismograph Networks*. https://doi.org/10.7914/SN/IU

Anderson, D. L. (1982). Hotspots, polar wander, Mesozoic convection and the geoid. *Nature*, *297*(5865), 391–393. https://doi.org/10.1038/297391a0

Arndt, N., Coltice, N., Helmstaedt, H., & Gregoire, M. (2009). Origin of Archean subcontinental lithospheric mantle: Some petrological constraints. *Lithos*, *109*(1–2), 61–71. https://doi.org/10.1016/j.lithos.2008.10.019

Artemieva, I. M. (2006). Global 1 x 1 thermal model TC1 for the continental lithosphere: Implications for lithosphere secular evolution. *Tectonophysics*, *416*(1–4), 245–277. https://doi.org/10.1016/j.tecto.2005.11.022

Bagheri, A., Khan, A., Al-Attar, D., Crawford, O., & Giardini, D. (2019). Tidal response of Mars constrained from laboratory-based viscoelastic dissipation models and geophysical data. *Journal of Geophysical Research: Planets*, *124*(11), 2703–2727. https://doi.org/10.1029/2019JE006015

Ball, P., White, N., Maclennan, J., & Stephenson, S. (2021). Global influence of mantle temperature and plate thickness on intraplate volcanism. *Nature Communications*, *12*(1), 2045. https://doi.org/10.1038/s41467-021-22323-9

Ballard, S., & Pollack, H. N. (1987). Diversion of heat by archean cratons: A model for Southern Africa. *Earth and Planetary Science Letters*, *85*(1–3), 253–264. https://doi.org/10.1016/0012-821x(87)90036-7

Bell, D. R., Schmitz, M. D., & Janney, P. E. (2003). Mesozoic thermal evolution of the Southern African mantle lithosphere. *Lithos*, *71*(2–4), 273–287. https://doi.org/10.1016/s0024-4937(03)00117-8

Bernstein, S., Kelemen, P. B., & Brooks, C. K. (1998). Depleted spinel Harzburgite xenoliths in Tertiary dykes from East Greenland: Restites from high degree melting. *Earth and Planetary Science Letters*, *154*(1–4), 221–235. https://doi.org/10.1016/s0012-821x(97)00175-1

Bina, C. R., & Helffrich, G. (1994). Phase transition Clapeyron slopes and transition zone seismic discontinuity topography. *Journal of Geophysical Research*, *99*(B8), 15853–15860. https://doi.org/10.1029/94jb00462

Bissig, F., Khan, A., & Giardini, D. (2022). Evidence for basalt enrichment in the mantle transition zone from inversion of triplicated P-and S-waveforms. *Earth and Planetary Science Letters*, *580*, 117387. https://doi.org/10.1016/j.epsl.2022.117387

Bissig, F., Khan, A., & Giardini, D. (2023). Joint inversion of PP and SS precursor waveforms and Rayleigh wave phase velocities for global mantle transition zone structure. *Geophysical Journal International*, *233*(1), 316–337. https://doi.org/10.1093/gji/ggac451

Bissig, F., Khan, A., Tauzin, B., Sossi, P. A., Munch, F., & Giardini, D. (2021). Multifrequency inversion of Ps and Sp receiver functions: Methodology and application to USarray data. *Journal of Geophysical Research: Solid Earth*, *126*(2), e2020JB020350. https://doi.org/10.1029/2020jb020350

Bock, G. (1994). Multiples as precursors to s, SKS and SCS. *Geophysical Journal International*, *119*(2), 421–427. https://doi.org/10.1111/j.1365-246x.1994.tb00132.x

Borgeaud, A. F., Kawai, K., & Geller, R. J. (2019). Three-dimensional S velocity structure of the mantle transition zone beneath Central America and the Gulf of Mexico inferred using waveform inversion. *Journal of Geophysical Research: Solid Earth*, *124*(9), 9664–9681. https://doi.org/10.1029/2018jb016924

Boyd, F. (1973). A pyroxene Geotherm. *Geochimica et Cosmochimica Acta*, *37*(2533), 2546. https://doi.org/10.1016/0016-7037(73)90263-9

Boyd, F., & McCallister, R. (1976). Densities of fertile and sterile garnet peridotites. *Geophysical Research Letters*, *3*(9), 509–512. https://doi.org/10.1029/gl003i009p00509

Boyd, F., Pearson, D., Hoal, K. O., Hoal, B., Nixon, P., Kingston, M., & Mertzman, S. (2004). Garnet Lherzolites from Louwrensia, Namibia: Bulk composition and P/T relations. *Lithos*, *77*(1–4), 573–592. https://doi.org/10.1016/j.lithos.2004.03.010

Boyd, F., Pokhilenko, N., Pearson, D., Mertzman, S., Sobolev, N., & Finger, L. (1997). Composition of the Siberian Cratonic mantle: Evidence from Udachnaya peridotite xenoliths. *Contributions to Mineralogy and Petrology*, *128*(2–3), 228–246. https://doi.org/10.1007/s004100050305

Braun, J. (2010). The many surface expressions of mantle dynamics. *Nature Geoscience*, *3*(12), 825–833. https://doi.org/10.1038/ngeo1020

Calò, M., Bodin, T., & Romanowicz, B. (2016). Layered structure in the upper mantle across North America from joint inversion of long and short period seismic data. *Earth and Planetary Science Letters*, *449*, 164–175. https://doi.org/10.1016/j.epsl.2016.05.054

Cammarano, F., Romanowicz, B., Stixrude, L., Lithgow-Bertelloni, C., & Xu, W. (2009). Inferring the thermochemical structure of the upper mantle from seismic data. *Geophysical Journal International*, *179*(2), 1169–1185. https://doi.org/10.1111/j.1365-246x.2009.04338.x

Canil, D. (2004). Mildly incompatible elements in peridotites and the origins of mantle lithosphere. *Lithos*, *77*(1–4), 375–393. https://doi.org/10.1016/j.lithos.2004.04.014

Carlson, R., Pearson, D., & James, D. (2005). Physical, chemical, and chronological characteristics of continental mantle. *Reviews of Geophysics*, *43*(1). https://doi.org/10.1029/2004rg000156

Chambers, K., Deuss, A., & Woodhouse, J. (2005). Reflectivity of the 410-km discontinuity from PP and SS precursors. *Journal of Geophysical Research*, *110*(B2). https://doi.org/10.1029/2004jb003345

Coltice, N., Gérault, M., & Ulvrová, M. (2017). A mantle convection perspective on global tectonics. *Earth-Science Reviews*, *165*, 120–150. https://doi.org/10.1016/j.earscirev.2016.11.006

Connolly, J. (2009). The geodynamic equation of state: What and how [Software]. *Geochemistry, Geophysics, Geosystems*, *10*(10). https://doi.org/10.1029/2009gc002540

Connolly, J., & Khan, A. (2016). Uncertainty of mantle geophysical properties computed from phase equilibrium models. *Geophysical Research Letters*, *43*(10), 5026–5034. https://doi.org/10.1002/2016gl068239

Cooper, C. M., Lenardic, A., & Moresi, L. (2006). Effects of continental insulation and the partitioning of heat producing elements on the Earth's heat loss. *Geophysical Research Letters*, *33*(13). https://doi.org/10.1029/2006gl026291

Doucet, L., Peslier, A., Ionov, D., Brandon, A., Golovin, A., Goncharov, A., & Ashchepkov, I. (2014). High water contents in the Siberian Cratonic mantle linked to metasomatism: An FTIR study of Udachnaya peridotite xenoliths. *Geochimica et Cosmochimica Acta*, *137*, 159–187. https://doi.org/10.1016/j.gca.2014.04.011

Doucet, L., Xu, Y., Klaessens, D., Hui, H., Ionov, D., & Mattielli, N. (2020). Decoupled water and iron enrichments in the cratonic mantle: A study on peridotite xenoliths from Tok, SE Siberian craton. *American Mineralogist*, *105*(6), 803–819. https://doi.org/10.2138/am-2020-7316

Durand, S., Debayle, E., & Ricard, Y. (2015). Rayleigh wave phase velocity and error maps up to the fifth overtone. *Geophysical Research Letters*, *42*(9), 3266–3272. https://doi.org/10.1002/2015gl063700

Duvernay, T., Davies, D. R., Mathews, C. R., Gibson, A. H., & Kramer, S. C. (2022). Continental magmatism: The surface manifestation of dynamic interactions between Cratonic lithosphere, mantle plumes and edge-driven convection. *Geochemistry, Geophysics, Geosystems*, *23*(7), e2022GC010363. https://doi.org/10.1029/2022gc010363

Dziewonski, A. M., & Anderson, D. L. (1981). Preliminary reference Earth model. *Physics of the Earth and Planetary Interiors*, *25*(4), 297–356. https://doi.org/10.1016/0031-9201(81)90046-7

Dziewonski, A. M., Chou, T.-A., & Woodhouse, J. H. (1981). Determination of earthquake source parameters from waveform data for studies of global and regional seismicity. *Journal of Geophysical Research*, *86*(B4), 2825–2852. https://doi.org/10.1029/jb086ib04p02825

Eeken, T., Goes, S., Pedersen, H., Arndt, N., & Bouilhol, P. (2018). Seismic evidence for depth-dependent metasomatism in cratons. *Earth and Planetary Science Letters*, *491*, 148–159. https://doi.org/10.1016/j.epsl.2018.03.018

Eeken, T., Goes, S., Petrescu, L., & Altoe, I. (2020). Lateral variations in thermochemical structure of the Eastern Canadian Shield. *Journal of Geophysical Research: Solid Earth*, *125*(7), e2019JB018734. https://doi.org/10.1029/2019jb018734

Efron, B., & Tibshirani, R. (1991). Statistical data analysis in the computer age. *Science*, *253*(5018), 390–395. https://doi.org/10.1126/science.253.5018.390

Eggler, D. H., McCallum, M., & Kirkley, M. (1987). Kimberlite-transported nodules from Colorado-Wyoming. *A record of enrichment of shallow portions of an infertile lithosphere: Geological Society of America Special Paper*, *215*, 77–90.

Ekström, G., Nettles, M., & Dziewoński, A. (2012). The global CMT project 2004–2010: Centroid-moment tensors for 13,017 earthquakes. *Physics of the Earth and Planetary Interiors*, *200*, 1–9.

Eulenfeld, T. (2020). Rf: Receiver function calculation in seismology [Software]. *Journal of Open Source Software*, *5*(48). https://doi.org/10.21105/joss.01808

Finnerty, A., & Boyd, F. (1987). Thermobarometry for garnet peridotite xenoliths: A basis for upper mantle stratigraphy. *Mantle Xenoliths. Wiley*, 381–402.

Fuchs, K., & Müller, G. (1971). Computation of synthetic seismograms with the reflectivity method and comparison with observations [Software]. *Geophysical Journal International*, *23*(4), 417–433. https://doi.org/10.1111/j.1365-246X.1971.tb01834.x

Fullea, J., Lebedev, S., Martinec, Z., & Celli, N. (2021). WINTERC-G: Mapping the upper mantle thermochemical heterogeneity from coupled geophysical–petrological inversion of seismic waveforms, heat flow, surface elevation and gravity satellite data. *Geophysical Journal International*, *226*(1), 146–191. https://doi.org/10.1093/gji/ggab094

Garber, J. M., Maurya, S., Hernandez, J.-A., Duncan, M. S., Zeng, L., Zhang, H. L., et al. (2018). Multidisciplinary constraints on the abundance of diamond and Eclogite in the cratonic lithosphere. *Geochemistry, Geophysics, Geosystems*, *19*(7), 2062–2086. https://doi.org/10.1029/2018gc007534

GEOFON Data Centre. (1993). Geofon seismic network [Dataset]. *Deutsches GeoForschungsZentrum GFZ*. https://doi.org/10.14470/TR560404

Geoscience Australia. (2021). Australian national seismograph network data collection [Dataset]. *Commonwealth of Australia (Geoscience Australia)*. https://doi.org/10.26186/144675

Glasgow, M. E., Zhang, H., Schmandt, B., Zhou, W.-Y., & Zhang, J. (2024). Global variability of the composition and temperature at the 410-km discontinuity from receiver function analysis of dense arrays. *Earth and Planetary Science Letters*, *643*, 118889. https://doi.org/10.1016/j.epsl.2024.118889

Grand, S. P. (2002). Mantle shear–wave tomography and the fate of subducted slabs. *Philosophical Transactions of the Royal Society of London, Series A: Mathematical, Physical and Engineering Sciences*, *360*(1800), 2475–2491. https://doi.org/10.1098/rsta.2002.1077

Griffin, W., O'Reilly, S., Abe, N., Aulbach, S., Davies, R., Pearson, N., et al. (2003). The origin and evolution of Archean lithospheric mantle. *Precambrian Research*, *127*(1–3), 19–41. https://doi.org/10.1016/s0301-9268(03)00180-3

Griffin, W., O'Reilly, S. Y., Afonso, J. C., & Begg, G. (2009). The composition and evolution of lithospheric mantle: A re-evaluation and its tectonic implications. *Journal of Petrology*, *50*(7), 1185–1204. https://doi.org/10.1093/petrology/egn033

Gurnis, M., & Hager, B. H. (1988). Controls of the structure of subducted slabs. *Nature*, *335*(6188), 317–321. https://doi.org/10.1038/335317a0

Hansen, N., Ros, R., Mauny, N., Schoenauer, M., & Auger, A. (2011). Impacts of invariance in search: When CMA-ES and PSO face ill-conditioned and non-separable problems. *Applied Soft Computing*, *11*(8), 5755–5769. https://doi.org/10.1016/j.asoc.2011.03.001

Harris, C. R., Millman, K. J., van der Walt, S. J., Gommers, R., Virtanen, P., Cournapeau, D., et al. (2020). Array programming with NumPy [Software]. *Nature*, *585*(7825), 357–362. https://doi.org/10.1038/s41586-020-2649-2

Harte, B., & Freer, R. (1982). Diffusion data and their bearing on the interpretation of mantle nodules and the evolution of the mantle lithosphere. In *International Kimberlite Conference: Extended abstracts* (Vol. 3, pp. 273–275).

Helffrich, G. (2000). Topography of the transition zone seismic discontinuities. *Reviews of Geophysics*, *38*(1), 141–158. https://doi.org/10.1029/1999rg000060

Heron, P., & Lowman, J. (2011). The effects of supercontinent size and thermal insulation on the formation of mantle plumes. *Tectonophysics*, *510*(1–2), 28–38. https://doi.org/10.1016/j.tecto.2011.07.002

Herzberg, C. (2004a). Geodynamic information in peridotite petrology. *Journal of Petrology*, *45*(12), 2507–2530. https://doi.org/10.1093/petrology/egh039

Herzberg, C. (2004b). Partial crystallization of mid-ocean ridge basalts in the crust and mantle. *Journal of Petrology*, *45*(12), 2389–2405. https://doi.org/10.1093/petrology/egh040

Herzberg, C., & Gazel, E. (2009). Petrological evidence for secular cooling in mantle plumes. *Nature*, *458*(7238), 619–622. https://doi.org/10.1038/nature07857

Herzberg, C., & O'hara, M. (2002). Plume-associated ultramafic magmas of phanerozoic age. *Journal of Petrology*, *43*(10), 1857–1883. https://doi.org/10.1093/petrology/43.10.1857

Hirose, K., & Kawamoto, T. (1995). Hydrous partial melting of Lherzolite at 1 GPA: The effect of H_2O on the genesis of basaltic magmas. *Earth and Planetary Science Letters*, *133*(3–4), 463–473. https://doi.org/10.1016/0012-821x(95)00096-u

Hosseini, K., & Sigloch, K. (2017). ObspyDMT: A Python toolbox for retrieving and processing large seismological data sets. *Solid Earth*, *8*(5), 1047–1070. https://doi.org/10.5194/se-8-1047-2017

Hunter, J., & Dale, D. (2007). The Matplotlib user's guide [Software]. *Matplotlib 0.90. 0 user's Guide*. https://matplotlib.org/stable/users/explain/quick_start.html

Institut de physique du globe de Paris (IPGP), & École et Observatoire des Sciences de la Terre de Strasbourg (EOST). (1982). Geoscope, French global network of broad band seismic stations [Dataset]. *Institut de physique du globe de Paris (IPGP)*. https://doi.org/10.18715/GEOSCOPE.G

Ionov, D. (2002). Mantle structure and rifting processes in the Baikal–Mongolia region: Geophysical data and evidence from xenoliths in volcanic rocks. *Tectonophysics*, *351*(1–2), 41–60. https://doi.org/10.1016/s0040-1951(02)00124-5

Ionov, D., Doucet, L., & Ashchepkov, I. (2010). Composition of the lithospheric mantle in the Siberian craton: New constraints from fresh peridotites in the Udachnaya-East kimberlite. *Journal of Petrology*, *51*(11), 2177–2210. https://doi.org/10.1093/petrology/egq053

IRIS Transportable Array. (2003). Usarray transportable array [Dataset]. *International Federation of Digital Seismograph Networks*. https://doi.org/10.7914/SN/TA

Jackson, I., & Faul, U. H. (2010). Grainsize-sensitive viscoelastic relaxation in olivine: Towards a robust laboratory-based model for seismological application. *Physics of the Earth and Planetary Interiors*, *183*(1–2), 151–163. https://doi.org/10.1016/j.pepi.2010.09.005

Jain, C., Rozel, A., & Tackley, P. (2019). Quantifying the correlation between mobile continents and elevated temperatures in the subcontinental mantle. *Geochemistry, Geophysics, Geosystems*, *20*(3), 1358–1386. https://doi.org/10.1029/2018gc007586

Jaques, A., O'Neill, H. S. C., Smith, C., Moon, J., & Chappell, B. (1990). Diamondiferous peridotite xenoliths from the Argyle (AK1) Lamproite Pipe, Western Australia. *Contributions to Mineralogy and Petrology*, *104*(3), 255–276. https://doi.org/10.1007/bf00321484

Jordan, T. H. (1978). Composition and development of the continental tectosphere. *Nature*, *274*(5671), 544–548. https://doi.org/10.1038/274544a0

Katsura, T. (2022). A revised adiabatic temperature profile for the mantle. *Journal of Geophysical Research: Solid Earth*, *127*(2), e2021JB023562. https://doi.org/10.1029/2021jb023562

Kemper, J., van Driel, M., Munch, F., Khan, A., & Giardini, D. (2022). A spectral element approach to computing normal modes. *Geophysical Journal International*, *229*(2), 915–932. https://doi.org/10.1093/gji/ggab476

Khan, A., Boschi, L., & Connolly, J. (2009). On mantle chemical and thermal heterogeneities and anisotropy as mapped by inversion of global surface wave data. *Journal of Geophysical Research*, *114*(B9). https://doi.org/10.1029/2009jb006399

Khan, A., Zunino, A., & Deschamps, F. (2013). Upper mantle compositional variations and discontinuity topography imaged beneath Australia from Bayesian inversion of surface-wave phase velocities and thermochemical modeling. *Journal of Geophysical Research: Solid Earth*, *118*(10), 5285–5306. https://doi.org/10.1002/jgrb.50304

Kind, R., Yuan, X., & Kumar, P. (2012). Seismic receiver functions and the lithosphere–asthenosphere boundary. *Tectonophysics*, *536*, 25–43. https://doi.org/10.1016/j.tecto.2012.03.005

Kinzler, R. J., & Grove, T. L. (1992). Primary magmas of mid-ocean ridge basalts 1. Experiments and methods. *Journal of Geophysical Research*, *97*(B5), 6885–6906. https://doi.org/10.1029/91jb02840

Kopylova, M., & Russell, J. (2000). Chemical stratification of cratonic lithosphere: Constraints from the Northern Slave craton, Canada. *Earth and Planetary Science Letters*, *181*(1–2), 71–87. https://doi.org/10.1016/s0012-821x(00)00187-4

Kopylova, M., Russell, J., & Cookenboo, H. (1999). Petrology of peridotite and Pyroxenite xenoliths from the Jericho kimberlite: Implications for the thermal state of the mantle beneath the Slave craton, Northern Canada. *Journal of Petrology*, *40*(1), 79–104. https://doi.org/10.1093/petroj/40.1.79

Korenaga, J. (2018). Crustal evolution and mantle dynamics through Earth history. *Philosophical Transactions of the Royal Society A: Mathematical, Physical & Engineering Sciences*, *376*(2132), 20170408. https://doi.org/10.1098/rsta.2017.0408

Langston, C. A. (1979). Structure under Mount Rainier, Washington, inferred from teleseismic body waves. *Journal of Geophysical Research*, *84*(B9), 4749–4762. https://doi.org/10.1029/jb084ib09p04749

Laske, G., Masters, G., Ma, Z., & Pasyanos, M. (2013). Update on CRUST1.0 – a 1-degree global model of Earth's crust. In *Geophysical Research Abstracts* (Vol. 15).2658

Lau, H. C., & Faul, U. H. (2019). Anelasticity from seismic to tidal timescales: Theory and observations. *Earth and Planetary Science Letters*, *508*, 18–29. https://doi.org/10.1016/j.epsl.2018.12.009

Lawrence, J. F., & Shearer, P. M. (2006a). Constraining seismic velocity and density for the mantle transition zone with reflected and transmitted waveforms. *Geochemistry, Geophysics, Geosystems*, *7*(10). https://doi.org/10.1029/2006gc001339

Lawrence, J. F., & Shearer, P. M. (2006b). A global study of transition zone thickness using receiver functions. *Journal of Geophysical Research*, *111*(B6). https://doi.org/10.1029/2005jb003973

Lazarov, M., Woodland, A. B., & Brey, G. P. (2009). Thermal state and redox conditions of the Kaapvaal mantle: A study of xenoliths from the Finsch mine, South Africa. *Lithos*, *112*, 913–923. https://doi.org/10.1016/j.lithos.2009.03.035

Lebedev, S., Fullea, J., Xu, Y., & Bonadio, R. (2024). Seismic thermography. *Bulletin of the Seismological Society of America*, *114*(3), 1227–1242. https://doi.org/10.1785/0120230245

Lee, C.-T., Luffi, P., & Chin, E. (2011). Building and destroying continental mantle. *Annual Review of Earth and Planetary Sciences*, *39*(1), 59–90. https://doi.org/10.1146/annurev-earth-040610-133505

Lee, C.-T., & Rudnick, R. L. (1999). Compositionally stratified cratonic lithosphere: Petrology and geochemistry of peridotite xenoliths from the Labait tuff cone, Tanzania. In *Proceedings of the 7th International Kimberlite Conference* (pp. 503–521).

Lenardic, A., & Moresi, L. (2001). Heat flow scaling for mantle convection below a conducting lid: Resolving seemingly inconsistent modeling results regarding continental heat flow. *Geophysical Research Letters*, *28*(7), 1311–1314. https://doi.org/10.1029/2000gl008484

Lenardic, A., Moresi, L., Jellinek, A., O'neill, C., Cooper, C., & Lee, C. (2011). Continents, supercontinents, mantle thermal mixing, and mantle thermal isolation: Theory, numerical simulations, and laboratory experiments. *Geochemistry, Geophysics, Geosystems*, *12*(10). https://doi.org/10.1029/2011gc003663

Lenardic, A., Moresi, L.-N., Jellinek, A., & Manga, M. (2005). Continental insulation, mantle cooling, and the surface area of oceans and continents. *Earth and Planetary Science Letters*, *234*(3–4), 317–333. https://doi.org/10.1016/j.epsl.2005.01.038

Ligorria, J. P., & Ammon, C. J. (1999). Iterative deconvolution and receiver-function estimation. *Bulletin of the Seismological Society of America*, *89*(5), 1395–1400. https://doi.org/10.1785/bssa0890051395

McCarthy, C., Takei, Y., & Hiraga, T. (2011). Experimental study of attenuation and dispersion over a broad frequency range: 2. The universal scaling of polycrystalline materials. *Journal of Geophysical Research*, *116*(B9), B09207. https://doi.org/10.1029/2011jb008384
McKenzie, D., & Bickle, M. (1988). The volume and composition of melt generated by extension of the lithosphere. *Journal of Petrology*, *29*(3), 625–679. https://doi.org/10.1093/petrology/29.3.625
Meier, U., Trampert, J., & Curtis, A. (2009). Global variations of temperature and water content in the mantle transition zone from higher mode surface waves. *Earth and Planetary Science Letters*, *282*(1–4), 91–101.
Menzies, M., & Hawkesworth, C. (1986). *Mantle metasomatism*. Academic Press Inc. Retrieved from https://www.osti.gov/biblio/5870369
Morgan, P. (1984). The thermal structure and thermal evolution of the continental lithosphere. *Physics and Chemistry of the Earth*, *15*, 107–193. https://doi.org/10.1016/0079-1946(84)90006-5
Mosegaard, K., & Tarantola, A. (1995). Monte Carlo sampling of solutions to inverse problems. *Journal of Geophysical Research*, *100*(B7), 12431–12447. https://doi.org/10.1029/94jb03097
Muller, G. (1985). The reflectivity method—a tutorial. *Journal of Geophysics-Zeitschrift Fur Geophysik*, *58*(1–3), 153–174.
Munch, F. (2024). Evidence for mantle thermo-chemical uniformity beneath cratons [data and models collection]. https://doi.org/10.3929/ethz-b-000678017
Munch, F., Khan, A., Tauzin, B., van Driel, M., & Giardini, D. (2020). Seismological evidence for thermo-chemical heterogeneity in Earth's continental mantle. *Earth and Planetary Science Letters*, *539*, 116240. https://doi.org/10.1016/j.epsl.2020.116240
Munch, F., Khan, A., Tauzin, B., Zunino, A., & Giardini, D. (2018). Stochastic inversion of P-to-s converted waves for mantle composition and thermal structure: Methodology and application. *Journal of Geophysical Research: Solid Earth*, *123*(12). https://doi.org/10.1029/2018jb016032
Natural Resources Canada. (1975). Canadian national seismograph network [Dataset]. *International Federation of Digital Seismograph Networks*. https://doi.org/10.7914/SN/CN
Nimis, P., & Grütter, H. (2010). Internally consistent geothermometers for garnet peridotites and pyroxenites. *Contributions to Mineralogy and Petrology*, *159*(3), 411–427. https://doi.org/10.1007/s00410-009-0455-9
Nixon, P., Rogers, N., Gibson, I., & Grey, A. (1981). Depleted and fertile mantle xenoliths from Southern African kimberlites. *Annual Review of Earth and Planetary Sciences*, *9*(1), 285–309. https://doi.org/10.1146/annurev.ea.09.050181.001441
Nyblade, A. A., & Pollack, H. N. (1993). A global analysis of heat flow from Precambrian terrains: Implications for the thermal structure of Archean and Proterozoic lithosphere. *Journal of Geophysical Research*, *98*(B7), 12207–12218. https://doi.org/10.1029/93jb00521
Pearson, D. (1999). The age of continental roots. *Lithos*, *48*(1–4), 171–194. https://doi.org/10.1016/s0419-0254(99)80011-1
Pearson, D., Canil, D., & Shirey, S. (2003). Mantle samples included in volcanic rocks: Xenoliths and diamonds. *Treatise on geochemistry*, *2*, 568.
Pearson, D., Scott, J., Liu, J., Schaeffer, A., Wang, L., van Hunen, J., et al. (2021). Deep continental roots and cratons. *Nature*, *596*(7871), 199–210. https://doi.org/10.1038/s41586-021-03600-5
Phillips, B. R., & Bunge, H.-P. (2005). Heterogeneity and time dependence in 3D spherical mantle convection models with continental drift. *Earth and Planetary Science Letters*, *233*(1–2), 121–135. https://doi.org/10.1016/j.epsl.2005.01.041
Priestley, K., Ho, T., Takei, Y., & McKenzie, D. (2024). The thermal and anisotropic structure of the top 300 km of the mantle. *Earth and Planetary Science Letters*, *626*, 118525. https://doi.org/10.1016/j.epsl.2023.118525
Priestley, K., & McKenzie, D. (2006). The thermal structure of the lithosphere from shear wave velocities. *Earth and Planetary Science Letters*, *244*(1–2), 285–301. https://doi.org/10.1016/j.epsl.2006.01.008
Priestley, K., & McKenzie, D. (2013). The relationship between shear wave velocity, temperature, attenuation and viscosity in the shallow part of the mantle. *Earth and Planetary Science Letters*, *381*, 78–91. https://doi.org/10.1016/j.epsl.2013.08.022
Qin, B., Ye, C., Liu, J., Huang, S., Wang, S., & ZhangZhou, J. (2024). Mapping global lithospheric mantle pressure-temperature conditions by machine-learning thermobarometry. *Geophysical Research Letters*, *51*(7), e2023GL106522. https://doi.org/10.1029/2023gl106522
Ritsema, J., Xu, W., Stixrude, L., & Lithgow-Bertelloni, C. (2009). Estimates of the transition zone temperature in a mechanically mixed upper mantle. *Earth and Planetary Science Letters*, *277*(1), 244–252. https://doi.org/10.1016/j.epsl.2008.10.024
Rolf, T., Coltice, N., & Tackley, P. (2012). Linking continental drift, plate tectonics and the thermal state of the Earth's mantle. *Earth and Planetary Science Letters*, *351*, 134–146. https://doi.org/10.1016/j.epsl.2012.07.011
Rondenay, S. (2009). Upper mantle imaging with array recordings of converted and scattered teleseismic waves. *Surveys in Geophysics*, *30*(4–5), 377–405. https://doi.org/10.1007/s10712-009-9071-5
Salmon, M., Balfour, N., & Sambridge, M. (2011). Australian seismometers in schools [Dataset]. *AusPass*. https://doi.org/10.7914/SN/S1
Schmandt, B. (2012). Mantle transition zone shear velocity gradients beneath USArray. *Earth and Planetary Science Letters*, *355*, 119–130. https://doi.org/10.1016/j.epsl.2012.08.031
Scripps Institution of Oceanography. (1986). Global seismograph network—Iris/IDA [Dataset]. *International Federation of Digital Seismograph Networks*. https://doi.org/10.7914/SN/II
Shapiro, N., & Ritzwoller, M. (2004). Thermodynamic constraints on seismic inversions. *Geophysical Journal International*, *157*(3), 1175–1188. https://doi.org/10.1111/j.1365-246x.2004.02254.x
Shorttle, O., Maclennan, J., & Lambart, S. (2014). Quantifying lithological variability in the mantle. *Earth and Planetary Science Letters*, *395*, 24–40. https://doi.org/10.1016/j.epsl.2014.03.040
Stixrude, L., & Lithgow-Bertelloni, C. (2011). Thermodynamics of mantle minerals-II. Phase equilibria. *Geophysical Journal International*, *184*(3), 1180–1213. https://doi.org/10.1111/j.1365-246x.2010.04890.x
Sun, S.-S., & McDonough, W. F. (1989). Chemical and isotopic systematics of oceanic basalts: Implications for mantle composition and processes. *Geological Society, London, Special Publications*, *42*(1), 313–345. https://doi.org/10.1144/gsl.sp.1989.042.01.19
Sundberg, M., & Cooper, R. F. (2010). A composite viscoelastic model for incorporating grain boundary sliding and transient diffusion creep; correlating creep and attenuation responses for materials with a fine Grain size. *Philosophical Magazine*, *90*(20), 2817–2840. https://doi.org/10.1080/14786431003746656
Takei, Y., Karasawa, F., & Yamauchi, H. (2014). Temperature, grain size, and chemical controls on Polycrystal Anelasticity over a broad frequency range extending into the seismic range. *Journal of Geophysical Research: Solid Earth*, *119*(7), 5414–5443. https://doi.org/10.1002/2014jb011146
Tappert, R., Foden, J., Muehlenbachs, K., & Wills, K. (2011). Garnet peridotite xenoliths and Xenocrysts from the Monk Hill kimberlite, South Australia: Insights into the lithospheric mantle beneath the Adelaide fold belt. *Journal of Petrology*, *52*(10), 1965–1986. https://doi.org/10.1093/petrology/egr036
Tarantola, A., & Valette, B. (1982). Generalized nonlinear inverse problems solved using the least squares criterion. *Reviews of Geophysics*, *20*(2), 219–232. https://doi.org/10.1029/rg020i002p00219

Tauzin, B., Debayle, E., & Wittlinger, G. (2008). The mantle transition zone as seen by global Pds phases: No clear evidence for a thin transition zone beneath hotspots. *Journal of Geophysical Research*, *113*(B8). https://doi.org/10.1029/2007jb005364

Tauzin, B., Kim, S., & Kennett, B. (2017). Pervasive seismic low-velocity zones within stagnant plates in the mantle transition zone: Thermal or compositional origin? *Earth and Planetary Science Letters*, *477*, 1–13. https://doi.org/10.1016/j.epsl.2017.08.006

Tauzin, B., Waszek, L., Ballmer, M. D., Afonso, J. C., & Bodin, T. (2022). Basaltic reservoirs in the Earth's mantle transition zone. *Proceedings of the National Academy of Sciences*, *119*(48), e2209399119. https://doi.org/10.1073/pnas.2209399119

Tian, D., Lv, M., Wei, S. S., Dorfman, S. M., & Shearer, P. M. (2020). Global variations of Earth's 520-and 560-km discontinuities. *Earth and Planetary Science Letters*, *552*, 116600. https://doi.org/10.1016/j.epsl.2020.116600

Toplis, M. (2005). The thermodynamics of iron and magnesium partitioning between olivine and liquid: Criteria for assessing and predicting equilibrium in natural and experimental systems. *Contributions to Mineralogy and Petrology*, *149*(1), 22–39. https://doi.org/10.1007/s00410-004-0629-4

Vinnik, L. (1977). Detection of waves converted from P to SV in the mantle. *Physics of the Earth and Planetary Interiors*, *15*(1), 39–45. https://doi.org/10.1016/0031-9201(77)90008-5

Virtanen, P., Gommers, R., Oliphant, T. E., Haberland, M., Reddy, T., Cournapeau, D., et al. (2020). SciPy 1.0: Fundamental algorithms for Scientific computing in Python [Software]. *Nature Methods*, *17*(3), 261–272. https://doi.org/10.1038/s41592-019-0686-2

Waszek, L., Tauzin, B., Schmerr, N. C., Ballmer, M. D., & Afonso, J. C. (2021). A poorly mixed mantle transition zone and its thermal state inferred from seismic waves. *Nature Geoscience*, *14*(12), 949–955. https://doi.org/10.1038/s41561-021-00850-w

Wilson, D. C., Angus, D., Ni, J. F., & Grand, S. P. (2006). Constraints on the interpretation of S-to-p receiver functions. *Geophysical Journal International*, *165*(3), 969–980. https://doi.org/10.1111/j.1365-246x.2006.02981.x

Woodland, A., & Koch, M. (2003). Variation in oxygen fugacity with depth in the upper mantle beneath the Kaapvaal craton, Southern Africa. *Earth and Planetary Science Letters*, *214*(1–2), 295–310. https://doi.org/10.1016/s0012-821x(03)00379-0

Xu, W., Lithgow-Bertelloni, C., Stixrude, L., & Ritsema, J. (2008). The effect of bulk composition and temperature on mantle seismic structure. *Earth and Planetary Science Letters*, *275*(1), 70–79.

Yan, J., Ballmer, M. D., & Tackley, P. J. (2020). The evolution and distribution of recycled oceanic crust in the Earth's mantle: Insight from geodynamic models. *Earth and Planetary Science Letters*, *537*, 116171. https://doi.org/10.1016/j.epsl.2020.116171

Yuan, X., Kind, R., Li, X., & Wang, R. (2006). The S receiver functions: Synthetics and data example. *Geophysical Journal International*, *165*(2), 555–564. https://doi.org/10.1111/j.1365-246x.2006.02885.x

Zhang, H., Schmandt, B., Zhou, W.-Y., Zhang, J. S., & Maguire, R. (2022). A single 520 km discontinuity beneath the contiguous United States with pyrolitic seismic properties. *Geophysical Research Letters*, *49*(24), e2022GL101300. https://doi.org/10.1029/2022gl101300